Développement d'un modèle monocristallin poreux

Le modèle monocristallin développé et validé dans le **Chapitre 2** et le **Chapitre 3** nous permet de simuler le comportement mécanique des aciers inoxydables austénitiques non-endommagés. Son utilisation est donc limitée car les matériaux fortement irradiés présentent souvent des cavités intragranulaires (**Section 1.2.3.3**). Pour intégrer l'effet de la porosité, on a besoin de développer un modèle monocristallin poreux.

Le présent chapitre est consacré au développement et à la validation d'un modèle de plasticité pour un monocristal poreux. Dans un premier temps, un critère de plasticité pour un monocristal poreux est développé analytiquement puis validé par les simulations numériques sur une cellule monocristalline poreuse, afin d'étudier le comportement d'un monocristal poreux. Dans un deuxième temps, le modèle monocristallin poreux est implémenté dans le code de calcul ZéBuLoN, ce qui permet d'homogénéiser les monocristaux en présence des cavités intragranulaires. Ce travail a fait l'objet d'une soumission de publication dans la revue « International Journal of Solids and Structures ».

4.1 Introduction aux modèles d'endommagement ductile

On présente ici brièvement les différents modèles permettant de modéliser la rupture ductile des matériaux. A l'opposé des matériaux fragiles, dont la rupture est caractérisée par une propagation très rapide des fissures en l'absence de déformation plastique macroscopique, les matériaux ductiles présentent progressivement un endommagement associé à une déformation plastique importante. Les principales étapes de la rupture ductile sont la nucléation, la croissance et la coalescence des cavités qui conduit à la rupture finale du matériau.

A partir des premiers travaux réalisés dans les années 60 [McClintock (1968) et Rice et Tracey (1969)], Gurson [Gurson (1977)] a proposé en premier une approche micromécanique à partir d'une analyse limite permettant d'obtenir la surface de charge macroscopique d'un milieu poreux avec une matrice rigide parfaitement plastique obéissant au critère de von Mises, en fonction de la fraction volumique d'une cavité sphérique. Ce modèle présente un fort couplage entre la déformation et l'endommagement. L'expression du critère de plasticité est donnée par :

$$\Phi = \frac{\sigma_{eq}^2}{\sigma_0^2} + 2f\cosh\left\{\frac{3\sigma_m}{2\sigma_0}\right\} - 1 - f^2 = 0 \qquad \text{Équation 4.1}$$

où σ_{eq} et σ_m présentent respectivement la contrainte équivalente macroscopique de von Mises et la contrainte hydrostatique (la trace du tenseur des contraintes), σ_0 est la limite d'écoulement plastique et f est la porosité.

Le modèle original de Gurson a été progressivement modifié et enrichi, soit de manière phénoménologique, soit de manière théorique, pendant ces trente dernières années, afin d'obtenir une meilleure description de sa formulation. Ici, on présente quelques-uns de ces modèles dont le formalisme pourra nous servir pour développer notre modèle monocristallin poreux présenté dans la section suivante.

- **Modèle de GTN** [Tvergaard et Needleman (1984)] : ce modèle propose une amélioration basée sur la simulation numérique [Tvergaard (1981)] en introduisant 2 coefficients différents q_1 et q_2. La contrainte équivalente d'écoulement σ^* est utilisée au lieu de la limite d'écoulement σ_0, afin de prendre en compte l'écrouissage du matériau poreux. De plus, pour prédire plus correctement la rupture finale du matériau, le modèle GTN introduit également une porosité effective f^* permettant de modéliser la phase de coalescence des cavités à partir d'une porosité critique f_c :

$$\Phi = \frac{\sigma_{eq}^2}{\sigma^{*2}} + 2q_1 f^* \cosh\left\{\frac{3}{2} q_2 \frac{\sigma_m}{\sigma^{*2}}\right\} - 1 - \left(q_1 f^*\right)^2 = 0 \qquad \text{Équation 4.2}$$

avec $f^*(f) = \begin{cases} f & \text{si } f \le f_c \\ f_c + \delta(f - f_c) & \text{si } f > f_c \end{cases}, \delta = \frac{f_u - f_c}{f_f - f_c}$. La porosité correspondant à la rupture finale du matériau est f_f pour laquelle $f^*(f_f) = f_u = 1/q_1$.

- **Modèle de Ponte-Castañeda-Suquet** [Ponte-Castañeda (1991) et Suquet (1992)] : ce modèle présente une borne inférieure de Hashin et Shtrikman au comportement non-linéaire en appliquant l'approche variationnelle, qui permet de mieux prédire le seuil de plastification dans les cas d'une faible triaxialité des contraintes (le rapport entre la contrainte hydrostatique et la contrainte équivalente) ou même sous chargement purement déviatorique ($\sigma_m = 0$) par rapport au modèle de Gurson :

$$\Phi = \left(1 + \frac{2}{3} f\right) \frac{\sigma_{eq}^2}{\sigma^{*2}} + \frac{9}{4} f \frac{\sigma_m^2}{\sigma^{*2}} - \left(1 - f\right)^2 = 0 \qquad \text{Équation 4.3}$$

- **Modèle de Leblond-Perrin-Suquet** [Leblond et al. (1994)] : il s'agit d'une extension phénoménologique du modèle de Gurson en combinant le critère présenté dans l'**Équation 4.3**, pour que le critère proposé puisse donner des bonnes solutions analytiques sous chargements hydrostatique ($\sigma_{eq} = 0$) et déviatorique ($\sigma_m = 0$) :

$$\Phi = \left(1 + \frac{2}{3} f\right) \frac{\sigma_{eq}^2}{\sigma^{*2}} + 2 f \cosh\left\{\frac{3\sigma_m}{2\sigma^*}\right\} - 1 - f^2 = 0 \qquad \text{Équation 4.4}$$

- **Modèle de Monchiet-Charkaluk-Kondo** [Monchiet et al. (2007)] : Le critère a été développé par l'utilisation de champs tests de vitesse de type Eshelby. Pour les faibles contraintes hydrostatiques σ_m, le développement limité d'ordre 1 du terme cosinus hyperbolique permet de retrouver la même expression que celle donnée dans l'**Équation 4.3** :

$$\Phi = \frac{\sigma_{eq}^2}{\sigma^{*2}} + 2f\cosh\left\{\frac{1}{\sigma^*}\sqrt{\frac{9}{4}\sigma_m^2 + \frac{2}{3}\sigma_{eq}^2}\right\} - 1 - f^2 = 0 \qquad \text{Équation 4.5}$$

- **Modèle de Benzerga-Besson** [Benzerga et Besson (2001)] : Différent des modèles présentés ci-dessus concernant les critères de plasticité d'un milieu poreux obéissant au critère de von Mises, le modèle de Benzerga-Besson permet de modéliser la surface de charge d'un matériau poreux orthotrope régi par le critère de Hill, en prenant en compte l'anisotropie plastique dans les équations constitutives :

$$\Phi = \frac{\sigma_{eq}^2}{\sigma^{*2}} + 2f\cosh\left\{\frac{\sqrt{3}}{2h_m}\frac{\sigma_m}{\sigma^*}\right\} - 1 - f^2 = 0 \qquad \text{Équation 4.6}$$

avec h_m le facteur d'anisotropie de la forme $h_m = \left[\frac{1}{4}\frac{h_1+h_2+4h_3}{h_1h_2+h_2h_3+h_3h_1} + \frac{1}{2h_6}\right]$, h_i les coefficients de Hill.

Afin de compléter le modèle de type Gurson, en appliquant la loi de normalité de l'écoulement plastique pour le matériau poreux, le tenseur taux de déformation plastique macroscopique effective s'écrit $\underline{\underline{\dot{\varepsilon}}}_p = \Lambda \partial\Phi / \partial\underline{\underline{\sigma}}$, avec Λ le multiplicateur plastique macroscopique [Gurson (1977)]. L'évolution de la déformation plastique effective p est donnée par l'équivalence des dissipations plastiques macroscopique effective du matériau poreux et microscopique de la matrice :

$$\underline{\underline{\sigma}} : \underline{\underline{\dot{\varepsilon}}}_p = (1-f)\sigma^* \dot{p} \qquad \text{Équation 4.7}$$

L'évolution de la porosité due à la croissance des cavités s'exprime par $\dot{f} = (1-f)\mathrm{trace}(\dot{\varepsilon}_p)$, en négligeant la partie élastique et en appliquant le principe de conservation de la masse.

Cependant, aucun des modèles présentés précédemment ne permet de représenter le comportement d'un monocristal poreux, car l'anisotropie complexe due à la cristallographie ne peut pas être décrite par le critère de von Mises, ni par le critère de Hill. De ce fait, il est nécessaire de développer un modèle permettant de modéliser explicitement le comportement macroscopique d'un monocristal poreux.

4.2 Proposition d'un critère de plasticité pour un monocristal poreux

Cette section présente le développement d'un critère de plasticité pour un monocristal poreux, en tenant compte de différents facteurs influençant le comportement macroscopique du matériau : l'orientation cristallographique, la triaxialité et la porosité.

Ce travail s'appuie sur le travail préliminaire effectué dans la thèse de S. Bugat [Bugat (2000)], qui propose une estimation permettant de réaliser une homogénéisation d'un monocristal visqueux non linéaire poreux. Cette approche consiste à estimer le potentiel du monocristal linéaire poreux de

comparaison, inspirée par l'application de l'approche variationnelle de type Hashin-Shtrikman [Debotton (1995)]. Nous adoptons un modèle de type Gurson en introduisant 3 coefficients α, q_1 et q_2, qui sont ajustés à partir des calculs numériques réalisés sur une cellule monocristalline tri-dimensionnelle parfaitement plastique contenant une cavité sphérique au milieu de la cellule.

D'après les résultats obtenus, on peut conclure que le critère de plasticité développé est capable de prédire la surface de charge d'un monocristal poreux pour des triaxialités comprises entre 0 et l'infini, en tenant compte des effets des directions du chargement principal et secondaire, ainsi que l'effet de la porosité pour une gamme comprise entre 0.005 et 0.1. Ce travail est décrit dans un article qui a été soumis à « International Journal of Solids and Structures » et qui est présenté ci-dessous.

A yield function for single crystals containing voids

X. Han[a,b,*], J. Besson[a], S. Forest[a], B. Tanguy[b], S. Bugat[c]

[a]*Centre des Matériaux, Mines ParisTech, UMR CNRS 7633, BP 87, 91003 Evry cedex, France*

[b]*Laboratoire de Comportement mécanique des Matériaux Irradiés, CEA Saclay, 91191 Gif-sur-Yvette cedex, France*

[c]*Département SI Finances-Gestion Groupe EDF, 75000 Paris, France*

Abstract

A yield function for single crystals containing voids has been developed based on a variational approach. This first yield function is phenomenologically extended by modifying the dependence on the mean stress and introducing three adjustable parameters. Unit cell finite element calculations are performed for various stress triaxiality ratios, main loading directions and porosity levels in the case of a perfectly plastic FCC single crystal. The three model parameters are adjusted on the unit cell calculations so that a very good agreement between simulation results and the proposed model is obtained.

Keywords: Porous media, Single crystal, Variational approach, Yield criterion, Unit cell model

1. Introduction

In crystalline metals, void nucleation, growth and coalescence lead to ductile fracture. Since the last forty years, building on the earliest works by Mc Clintock (1968), Rice and Tracey (1969), and Gurson (1977), much effort has been made to improve the prediction of damage evolution and fracture of porous ductile materials at macro and mesoscopic scales. The role of various characteristic features such as porosity, viscoplasticity, void shape, plastic anisotropy of the matrix has been studied. Some reviews were recently provided by Pineau and Pardoen (2007), Besson (2010), Benzerga and Leblond (2010). Two main approaches have been proposed to develop models for ductile damage growth. The first one is based on the seminal work by Gurson (1977) which uses an upper bound approach, following Tvergaard and Needleman (1984), Gologanu and Leblond (1993), Leblond et al. (1994), Benzerga and Besson (2001), Monchiet et al. (2007), Monchiet et al. (2008). The second approach is based on variational formulation of the homogenization theory using the concept of linear-comparison material, see Ponte Castañeda (1991), DeBotton and Ponte Castañeda (1995), Liu et al. (2005), Danas and Ponte Castañeda (2009) and Lebensohn et al. (2011).

Theoretical results obtained following these approaches can be verified using unit cell calculations first introduced in the pioneering work by Koplik and Needleman (1988). This versatile methodology allows to easily study the effect of various parameters on void growth and coalescence such as hardening rate (Faleskog et al., 1998, Gao et al., 1998, Lecarme et al., 2011), void shape or cell shape (Pardoen and Hutchinson, 2000), void population (Faleskog and Shih (1997), Fabrègue and Pardoen (2008) and Fritzen et al. (2012)), void distribution (Bandstra and Koss, 2008), and second phase particles (Steglich and Brocks, 1997, Steglich et al., 1999).

The effect of the anisotropy of matrix behaviour on void growth was investigated in relation to the anisotropic plastic properties of metal sheets, see in particular (Benzerga et al., 2004) and more recently (Monchiet et al., 2008). Typically, a Hill–type yield criterion was assumed for the matrix in the latter references. The situation is quite different in the presence of voids embedded in a single crystalline matrix. The case of single crystals containing voids (hereafter referred to as porous single crystals) has only been studied recently using the unit cell methodology either based on FE simulations (Schacht et al. (2003), Yerra et al. (2010), Ha and Kim (2010)), or based on slip line theory in the case of simple cylindrical voids (Kysar et al. (2005), Gan et al. (2006), Gan and Kysar (2007)). Besides, the analysis of ductile fracture in single crystals has been performed at smaller scales for nano and micro–voids by means of Discrete Dislocations Dynamics in (Huang et al. (2007), Hussein et al. (2008), Segurado and Llorca (2009), Segurado and Llorca (2010) and Huang et al. (2012)), and Molecular Dynamics in (Potirniche et al. (2006), Zhao et al. (2009), Traiviratana et al. (2008), Tang et al. (2010b) and Tang et al. (2010a)). However a set of constitutive equations describing the overall behaviour of porous single crystals is still lacking in the literature. The previously mentioned papers do not provide an overall yield function for porous single crystals. There is currently a real need for such a yield function that would be simple enough to allow straightforward Finite Element implementation for carrying out structural computations of ductile fracture in single and poly–crystals. It could be used for instance to reproduce experimental facts showing accelerated anisotropic growth of cavities in single crystals as observed in Crépin et al. (1996).

The purpose of the present work is to develop a model to describe the yield function of porous single crystals. Such models could be used to represent ductility of stainless steel (304/316 series) used for core internals of Fast Breeder Reactor and PWR nuclear power plants in which intragranular voids develop and lead to the phenomenon of swelling due to high irradiation levels (Foster and Strain (1974), Seran et al. (1984), Dubuisson (2011) and Renault et al. (2011)), also that of Ni based single crystal superalloys used in turbo-engines components (Wang et al., 2006). The model is theoretically motivated using a micromechanical analysis based on the variational approach by (Ponte Castañeda and Suquet, 1998). It is extended on a phenomenological basis to match trends obtained for rate-independent material (e.g. Gurson-Tvergaard-Needleman model). Unit

cell calculations are used to adjust and validate the model. Various loading directions and porosity levels (from 0.5% to 10%) are used.

The single crystal constitutive framework is recalled in section 2.1. The proposed yield function for porous single crystal is presented in section 2.2. The section 3 is dedicated to the identification methodology of the corresponding material parameters from unit cell computations. The results and validation of the approach are provided in section 4 in terms of crystal orientation, loading conditions and void volume fraction. The micromechanical motivation of the model is explained in Appendix A.

2. Proposed model for porous single crystals

The analysis given in this paper is limited to the small deformation framework, as it is the case in standard limit analysis.

2.1. Model for the single crystal matrix

In this work, which essentially deals with yielding of porous single crystals, a very simple law is used to describe the constitutive behaviour of the single crystal matrix. For each slip system $s = 1 \dots N$, the resolved shear stress, τ_s is expressed as:

$$\tau_s = \underline{\sigma} : \underline{m}_s \quad \text{with } \underline{m}_s = \frac{1}{2}\left(\vec{l}_s \otimes \vec{n}_s + \vec{n}_s \otimes \vec{l}_s\right) \tag{1}$$

where $\underline{\sigma}$ is the Cauchy stress tensor acting on the single crystal volume element. $\vec{l}_s$ and $\vec{n}_s$ are the unit vectors along the slip direction of the slip system s and normal to the slip plane, respectively. The total number of slip systems is N. For each slip system a yield surface can be defined as:

$$\psi_s = |\tau_s| - \tau_0 \tag{2}$$

Provided that $\psi_s \geq 0$, the slip rate for each slip system s is given as:

$$\dot{\gamma}_s(\tau_s) = \dot{\gamma}_0 \left(\frac{\psi_s}{\tau_0}\right)^n = \dot{\gamma}_0 \left(\frac{|\tau_s| - \tau_0}{\tau_0}\right)^n \tag{3}$$

where $\dot{\gamma}_0$, τ_0 and n are material parameters. τ_0 represents the critical resolved shear stress (CRSS) of the slip system. For the sake of simplicity each slip system is assumed to have the same CRSS but the model presented here can be easily extended in order to take into account different CRSS as well as self and cross hardening. Using the normality rule, the plastic strain rate tensor, $\underline{\dot{\varepsilon}}_p$, is expressed as:

$$\underline{\dot{\varepsilon}}_p = \sum_s \dot{\gamma}_s \frac{\partial \psi_s}{\partial \underline{\sigma}} = \sum_s \dot{\gamma}_s \text{sign}(\tau_s) \underline{m}_s \tag{4}$$

2.2. Model for the porous single crystal

One considers here a single crystal containing spherical voids. The void volume fraction is referred to as f in the following. Based on the variational formulation proposed by Ponte Castañeda and Suquet (1998), it is shown in Appendix A that an effective scalar resolved stress acting on each slip system $\tau_s^*(\underline{\sigma}, f)$ can be defined as a function of the applied stress and the porosity level, such that:

$$\tau_s^* - \frac{1}{1-f}\left(\tau_s^2 + \frac{2}{45}f\sigma_{eq}^2 + \frac{3}{20}f\sigma_m^2\right)^{\frac{1}{2}} \overset{\text{def. } \tau_s^*}{=} 0 \tag{5}$$

where σ_m (resp. σ_{eq}) is the mean stress (resp. von Mises stress) of the macroscopic stress tensor $\underline{\sigma}$. τ_s^{*2} is expressed as a quadratic form of $\underline{\sigma}$. Note that the notations used here for the overall yield functions are different from those in Appendix A: Small letters are used for the stress and strain quantities instead of capital letters, because there is no reference any more to the micromechanical variational analysis. Similar yield functions were obtained in the case of a voided solid made of an isotropic von Mises matrix (Leblond et al., 1994). The quadratic dependence in (5) is known to be inadequate in the case of plastic solids since the seminal works of Mc Clintock (1968) and Rice and Tracey (1969). An exponential dependence on the mean stress should be preferred. Using the second order Taylor expansion of $\cosh(x) = 1 + \frac{1}{2}x^2$, other definitions of the effective scalar resolved stress τ_s^* can be proposed so that it better corresponds to models derived from the Gurson (1977) model. Following the concept of a scalar stress measure (Besson et al., 2001), which can be explicitly or implicitly defined, another expression for τ_s^* can be worked out from the following expression which takes into account the mean stress dependence as in Gurson type models:

$$\left(\frac{\tau_s^2}{\tau_s^{*2}} + \frac{2}{45}f\frac{\sigma_{eq}^2}{\tau_s^{*2}}\right) + 2f\cosh\left(\sqrt{\frac{3}{20}}\frac{\sigma_m}{\tau_s^*}\right) - 1 - f^2 \overset{\text{def. } \tau_s^*}{=} 0 \tag{6}$$

τ_s^* is found by solving this equation. Another solution, based on the recent development by Monchiet et al. (2007) would be to define τ_s^* based on the following equation:

$$\frac{\tau_s^2}{\tau_s^{*2}} + 2f\cosh\left(\sqrt{\frac{3}{20}\frac{\sigma_m^2}{\tau_s^{*2}} + \frac{2}{45}\frac{\sigma_{eq}^2}{\tau_s^{*2}}}\right) - 1 - f^2 \overset{\text{def. } \tau_s^*}{=} 0 \tag{7}$$

In the following the Gurson-like formulation will be used (Eq. 6). It is however well known that the original Gurson (1977) model could not well represent the behaviour of actual voided cells as simulated using finite element calculations (Brocks et al. (1995), Kuna and Sun (1996) and Fritzen et al. (2012)) so that empirical modifications have to be introduced to better represent the cell behaviour (Tvergaard and Needleman (1984) and Faleskog et al. (1998)). Accordingly, the following definition for τ_s^* is proposed:

$$\left(\frac{\tau_s^2}{\tau_s^{*2}} + \alpha\frac{2}{45}f\frac{\sigma_{eq}^2}{\tau_s^{*2}}\right) + 2q_1f\cosh\left(q_2\sqrt{\frac{3}{20}}\frac{\sigma_m}{\tau_s^*}\right) - 1 - q_1^2f^2 \overset{\text{def. } \tau_s^*}{=} 0 \tag{8}$$

where α, q_1 and q_2 are parameters that need to be adjusted. q_1 and q_2 play a similar role as in the work by Tvergaard and Needleman (1984) whereas α is a new parameter weighting the relative contribution of the resolved shear stress on each slip system and the usual isotropic equivalent von Mises stress measure. The identification of these parameters will be done in the following based on unit cell simulations of voided single crystals. In all cases, $\tau_s^* = |\tau_s|$ for $f = 0$ so that the yield surface of the single crystal matrix is retrieved.

For each slip system, the yield surface is then defined as:

$$\psi_s^* = \tau_s^* - \tau_0 \geq 0 \tag{9}$$

The plastic strain rate tensor is still expressed using the normality rule as:

$$\underline{\dot{\varepsilon}}_p = (1-f)\sum_s \dot{\gamma}_s \frac{\partial \psi_s^*}{\partial \underline{\sigma}} = (1-f)\sum_s \dot{\gamma}_s \frac{\partial \tau_s^*}{\partial \underline{\sigma}} \tag{10}$$

where $\dot{\gamma}_s$ is obtained as a function of τ_s^* using Eq. 3 as:

$$\dot{\gamma}_s(\tau_s) = \dot{\gamma}_0 \left(\frac{\psi_s^*}{\tau_0}\right)^n = \dot{\gamma}_0 \left(\frac{\tau_s^* - \tau_0}{\tau_0}\right)^n \tag{11}$$

Whatever the chosen definition (Eqs. 5, 6, 7 or 8), the effective stress τ_s^* is an homogeneous function of $\underline{\sigma}$ of degree 1 and differentiable so that (Euler's theorem): $\partial \tau_s^* / \partial \underline{\sigma} : \underline{\sigma} = \tau_s^*$. The plastic dissipation is obtained as:

$$\underline{\dot{\varepsilon}}_p : \underline{\sigma} = (1-f)\sum_s \dot{\gamma}_s \frac{\partial \tau_s^*}{\partial \underline{\sigma}} : \underline{\sigma} = (1-f)\sum_s \dot{\gamma}_s \tau_s^* \geq 0 \tag{12}$$

which expresses the equality between the plastic work at the macroscopic level (left-hand side) and the microscopic level (right-hand side). The factor $(1-f)$ on the right-hand side corresponds to the volume fraction occupied by the single crystal matrix in which a power equal to $\sum_s \dot{\gamma}_s \tau_s^*$ is dissipated.

3. Model parameter determination based on finite element analysis

In this section, the proposed model (Eq. 8) will be tested and adjusted. Finite element calculations of voided unit cells are carried out. The adjustable model parameters (α, q_1 and q_2) will be identified to represent unit cell calculations results. In this work Face-Centered Cubic (FCC) single crystals are considered. In this highly-symmetric crystalline structure, plastic slip occurs on a group of 12 slip systems following $\{111\}\langle 110\rangle$ (see Tab. 1). Eq. 11, which relates the slip rate to the effective resolved stress, can be rewritten as:

$$\tau_s^* - \tau_0 - \tau_0 \left(\frac{\dot{\gamma}_s}{\dot{\gamma}_0}\right)^{\frac{1}{n}} = 0 \tag{13}$$

Slip system s	1	2	3	4	5	6	7	8	9	10	11	12
Slip plane $\vec{n}$	(111)			$(1\bar{1}1)$			$(\bar{1}11)$			$(11\bar{1})$		
Slip direction $\vec{l}$	$[\bar{1}01]$	$[0\bar{1}1]$	$[\bar{1}10]$	$[\bar{1}01]$	[011]	[110]	$[0\bar{1}1]$	[110]	[101]	$[\bar{1}10]$	[101]	[011]

Table 1: Slip systems in FCC single crystals

In the limiting case of a nearly perfectly plastic behaviour, which is used in this study, calculations are performed such that the viscous stress is less than 1% of the CRSS:

$$\tau_0 \left(\frac{\dot{\gamma}_s}{\dot{\gamma}_0} \right)^{\frac{1}{n}} < 1\% \times \tau_0 \tag{14}$$

within the usual range of imposed strain rates for engineering materials.

The material parameters for a FCC single crystal used for the unit cell analysis are given in Tab. 2. The elastoviscoplastic crystal plasticity model based on Schmid's law with a threshold requires the choice of elasticity moduli. The elastic moduli (cubic elasticity C_{11}, C_{12} and C_{44}) take here typical values for 300 series austenitic stainless steels at 340°C. However, as it is well–known in porous plasticity, the results of the limit analysis do not depend on the elastic properties of the material but only on the plasticity threshold value. This has been checked for unit cell computations with a single void but also for populations of interacting voids, for instance in Fritzen et al. (2012). The same feature has been checked here for crystal plasticity in the presented unit cell computations. The value of the parameter $\dot{\gamma}_0$ is chosen to satisfy the condition given in Eq. 14. The same threshold value $\tau_0 = 60$ MPa is considered for all slip systems in Schmid's law. Accordingly, activation of one slip system at a given Gauss point of the finite element mesh depends on the value of the resolved shear stress at this point. The 12 possible slip systems are considered at each material point. In the simulation, slip system activation is heterogeneous due to the presence of the hole. Multiple slip is allowed and takes place at several locations. Fully-implicit time integration method is used for the material's constitutive equations (Foerch et al., 1997).

C_{11}	C_{12}	C_{44}	τ_0	n	$\dot{\gamma}_0$
199 GPa	136 GPa	105 GPa	60 MPa	5	7.776 10^8 s^{-1}

Table 2: Material parameters for FE simulations

3.1. 3D finite element unit cell model

In the last decades, the FE simulation of unit cells has become a well-known simulation technique to investigate the global and local responses of heterogeneous materials (Needleman (1972), Tvergaard (1981), Tvergaard (1982), Koplik and Needleman (1988), Worswick and Pick (1990),

Quinn et al. (1997), Pardoen and Hutchinson (2000) and Benzerga and Besson (2001)). Three–dimensional unit cell calculations of porous media, considered as an homogenization method of a representative volume element (RVE) containing uniformly distributed voids, are widely applied to study the effect of various parameters such as multiaxial stress state, crystallographic orientation, and initial void volume fraction, on void growth (Liu et al. (2007), Yerra et al. (2010), Ha and Kim (2010) and Yu et al. (2010)) and coalescence (Kuna and Sun (1996), Zhang et al. (1999), Schacht et al. (2003), Liu et al. (2007), Liu et al. (2010), Yerra et al. (2010) and Liu et al. (2012)).

In this study, FE simulation of unit cells is used to determine the yield surface of porous single crystals depending on crystallographic orientation and void volume fraction. Results of the simulation are used to calibrate the model parameters (q_1, q_2 and α) introduced in the previous section Eq. 8. The FE mesh used for the simulation is shown in Fig. 1. The cubic cell (length l_0) contains a spherical void (radius r_0) located at the center of the cell. Except for specific crystallographic orientation the problem has no symmetry so that the full cell has to be meshed. The void volume fraction is simply given by: $f = V_{void}/V_{tot} = \frac{4}{3}\pi r_0^3/l_0^3$.

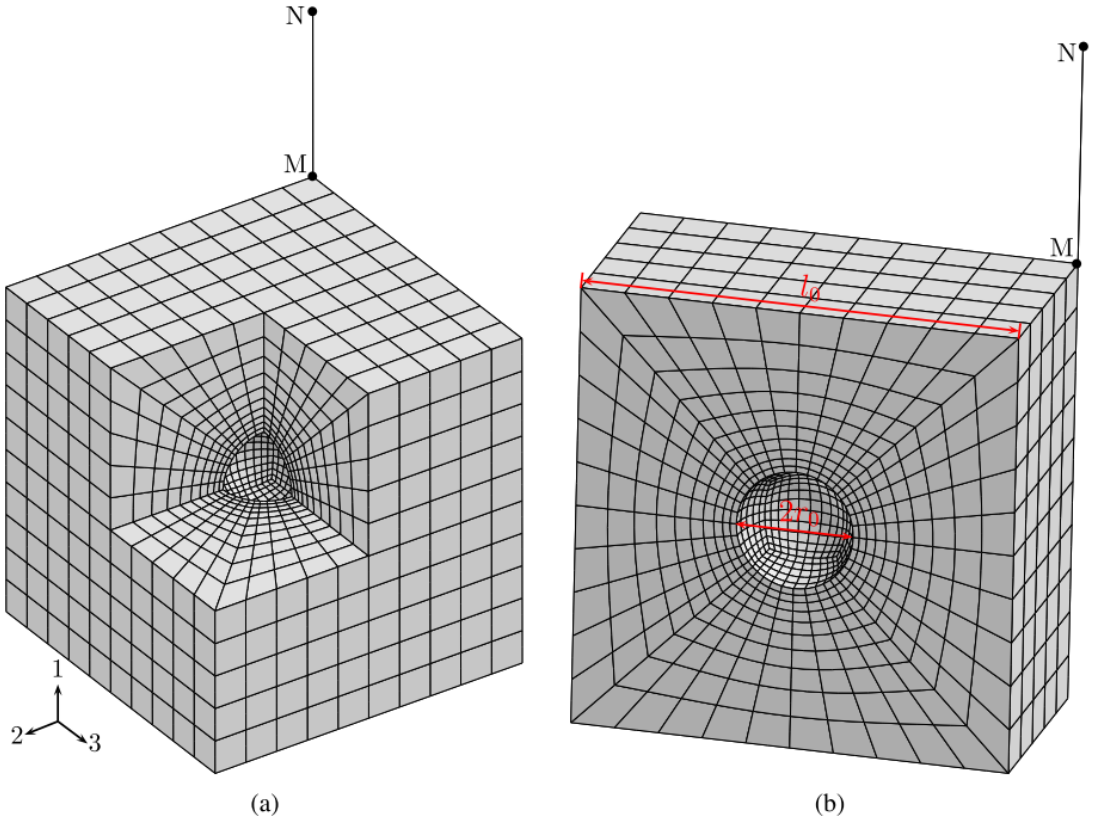

Figure 1: Unit cell with a spherical void in its center. (a) FE mesh for $f = 0.01$, with a cut of $1/8$ of the full geometry; (b) half of the full geometry showing the dimensions of the unit cell with a central void.

The 3D mesh is made of reduced-integrated quadratic hexahedral elements (see Fig. 1). The simulations were carried out using the Zset FE software (Besson and Foerch, 1998). A convergence study was also performed to optimize calculation time while keeping sufficient accuracy. Calculations are carried out so as to prescribe a constant overall stress triaxiality ratio (ratio of the mean stress to the von Mises stress). The overall macroscopic stress tensor is expressed in terms of 3 principal stresses as:

$$\underline{\sigma} = \begin{bmatrix} \sigma_1 & 0 & 0 \\ 0 & \sigma_2 & 0 \\ 0 & 0 & \sigma_3 \end{bmatrix} = \sigma_1 \begin{bmatrix} 1 & 0 & 0 \\ 0 & \eta_2 & 0 \\ 0 & 0 & \eta_3 \end{bmatrix} \tag{15}$$

where η_2 and η_3 are loading parameters which are kept constant for every single unit cell simulation. Both parameters vary between -0.5 and 1. It is assumed that $\sigma_1 > 0$. The stress triaxiality ratio is expressed as:

$$a = \frac{\sigma_m}{\sigma_{eq}} = \frac{1 + \eta_2 + \eta_3}{3\sqrt{1 - \eta_2 - \eta_3 - \eta_2\eta_3 + \eta_2^2 + \eta_3^2}} \tag{16}$$

As triaxiality shall be kept constant during the loading history, the parameters η_2 and η_3 have to remain constant whereas the ratios of mean strains E_{22}/E_{11} and E_{33}/E_{11} will vary in time. Two strategies were used to prescribe constant triaxiality. The first one uses the technique presented by Brocks et al. (1995). A special truss element (MN in Fig. 1) is added to the mesh. It acts as a spring in the main loading direction (i.e. **1**) which measures the mean stress component in that direction. A portion (η_2 and η_3) of this stress is then applied in both other directions **2** and **3**. Normal displacements on the cell faces are kept homogeneous so that the cell keeps a parallelipedic shape. This technique allows to perform displacement controlled FE simulations. It is suitable for highly symmetric crystal directions (e.g. **1** = [100], **2** = [010], **3** = [001]) but tends to over-constrain the model for general orientations so that high stresses are generated (in some cases stresses higher than the theoretical stresses for the undamaged single crystal are obtained). For this reason a second simulation technique assuming periodic boundary conditions was also used. The displacement vector $\vec{u}$ associated with each material point $\vec{x}$ takes the form :

$$\vec{u} = \underline{E} \cdot \vec{x} + \vec{v}, \ \forall \vec{x} \in V_{tot} \tag{17}$$

where $\underline{E}$ denotes the macroscopic strain tensor and $\vec{v}$ is the periodic fluctuation vector, which takes the same value for two points situated on opposite outer boundary surfaces ∂V_{tot} of the entire volume V_{tot}, while the traction vector $\vec{t} = \underline{\sigma} \cdot \vec{n}$ takes opposite values on these two points, with $\vec{n}$ being the outer unit normal vector on ∂V_{tot}. In the finite element implementation, the components of the macroscopic strain tensor, E_{ij}, are degrees of freedom and the associated reactions of which, R_{ij}, correspond to the macroscopic stress component Σ_{ij} times the cell volume: $R_{ij} = V_{tot} \times \Sigma_{ij}$, see (Besson et al., 2009). Simulations are then carried out prescribing the different reactions so

that $R_{22} = \eta_2 R_{11}$, $R_{33} = \eta_3 R_{11}$ and $R_{12} = R_{23} = R_{31} = 0$. In that case, simulations are load controlled.

Both methods (spring loaded cell and fully periodic cell) were compared in the case of highly symmetric triaxial loading (e.g. $[100]$–$[010]$–$[001]$). Results shown in Fig. 2 indicate that both methods result in almost identical results in this particular case. In the general case of non-symmetric orientations, spring loading conditions lead to an over-constraining effect so that slightly larger yield surfaces are generated. It is also shown that the stress levels quickly stabilize (due to the absence of work hardening). Based on these results, stress levels used to calibrate and validate the proposed yield function will be determined for a strain along direction **1** equal to 3%.

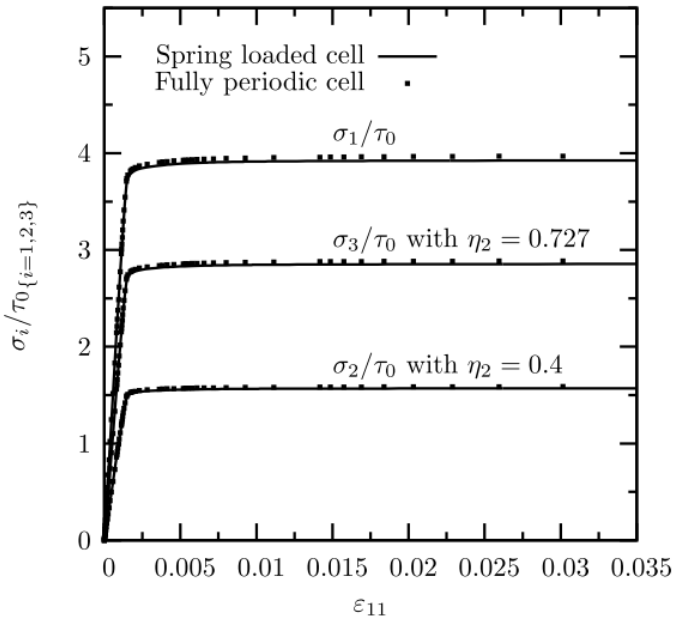

Figure 2: Normalized macroscopic stresses along the three principal loading directions as functions of the macroscopic deformation along direction **1** for **1** $= [100]$, **2** $= [010]$ and **3** $= [001]$ with $\eta_2 = 0.4$, $\eta_3 = 0.727$ and a porosity level $f = 0.01$.

3.2. Model parameter determination

In order to identify the model parameters from various numerical simulations for different crystallographic orientations, the proposed model can be written as:

$$\left(\frac{\left(\left(\underline{P}^T \cdot \underline{\sigma} \cdot \underline{P}\right) : \underline{m}_s\right)^2}{\tau_s^{*2}} + \alpha \frac{2f}{45}\frac{\sigma_{eq}^2}{\tau_s^{*2}}\right) + 2q_1 f \cosh\left(q_2\sqrt{\frac{3}{20}}\frac{\sigma_m}{\tau_s^*}\right) - 1 - (q_1 f)^2 \overset{\text{def. } \tau_s^*}{=} 0 \qquad (18)$$

where $\underline{\sigma}$ is the macroscopic stress tensor on global coordinates defined in Eq. 15 and $\underline{P}$ denotes the rotation matrix following **zxz** convention (Goldstein et al. (2002)), which turns global basis to crystal basis using Euler angles (ϕ_1, Φ, ϕ_2), given by:

$$\underline{P} = \begin{bmatrix} \cos\phi_1\cos\phi_2 - \sin\phi_1\cos\Phi\sin\phi_2 & \sin\phi_1\cos\phi_2 + \cos\phi_1\cos\Phi\sin\phi_2 & \sin\Phi\sin\phi_2 \\ -\cos\phi_1\sin\phi_2 - \sin\phi_1\cos\Phi\cos\phi_2 & -\sin\phi_1\sin\phi_2 + \cos\phi_1\cos\Phi\cos\phi_2 & \sin\Phi\cos\phi_2 \\ \sin\phi_1\sin\Phi & -\cos\phi_1\sin\Phi & \cos\Phi \end{bmatrix} \quad (19)$$

To validate the proposed model for single crystals, five crystallographic orientations for the main loading direction (direction **1**) have been chosen: $[100]$, $[110]$, $[111]$, $[210]$ and $[\bar{1}25]$. Another three cases are complemented to study the effect of secondary loading directions (directions **2** and **3**). All these cases are summarized in Tab. 3. Five porosity levels are considered as follows : f=0.005, 0.01, 0.02, 0.05 and 0.1.

Test number	Crystallographic orientation on global coordinates 1-2-3	Euler angles (°)		
		ϕ_1	Φ	ϕ_2
1	[100]-[010]-[001]	0	0	0
2	[100]-[01$\bar{1}$]-[011]	180	45	180
3	[100]-[02$\bar{1}$]-[012]	180	26.57	180
4	[110]-[$\bar{1}$10]-[001]	45	0	0
5	[111]-[$\bar{2}$11]-[0$\bar{1}$1]	0	45	54.74
6	[210]-[$\bar{1}$20]-[001]	26.57	0	0
7	[$\bar{1}$25]-[1$\bar{2}$1]-[210]	116.57	90	65.91
8	[$\bar{1}$25]-[0$\bar{5}$2]-[(29)25]	93.95	80.24	67.86

Table 3: Crystallographic orientations for numerical simulations and corresponding Euler angles.

Note that a special case with axisymmetric triaxial stress state ($\eta_2 = \eta_3 = \eta$) will also be investigated. In that case the stress triaxiality ratio is expressed as: $a = \frac{1}{3}(1+2\eta)/(1-\eta)$. The orthogonality of the three imposed principal stresses, the axisymmetric stress state and the symmetric crystalline structure of FCC materials allow deriving a simplified expression of the resolved shear stress on slip system s, which is then expressed as:

$$|\tau_s| = \left| \left(\underline{P}^T \cdot \underline{\sigma} \cdot \underline{P}\right) : \underline{m}_s \right| = F_s^{\mathbf{1}} \sigma_{eq} = F_s^{\mathbf{1}}(1-\eta)\sigma_1 \quad (20)$$

where $F_s^{\mathbf{1}}$ is the Schmid factor for slip system s obtained from a uniaxial tensile test on the matrix material along the main loading direction **1**. Hence, the resulting effective resolved stress τ_s^* for slip system s is given by:

$$\left(\left(F_s^{\mathbf{1}}\right)^2 + \alpha\frac{2f}{45}\right)\frac{(1-\eta)^2\sigma_1^2}{\tau_s^{*2}} + 2q_1 f\cosh\left(\frac{q_2}{2}\sqrt{\frac{1}{15}}\frac{(1+2\eta)\sigma_1}{\tau_s^*}\right) - 1 - (q_1 f)^2 \overset{\text{def. } \tau_s^*}{=} 0 \quad (21)$$

Based on this equation, the whole range of positive stress triaxiality from zero to infinity will be investigated. In FE simulations, ten distributed values of triaxialities have been chosen to test the proposed model (see Tab. 4).

a	0	0.33	0.5	1.0	1.5	3.0	5.0	10.0	50.0	$+\infty$
η	-0.5	0	0.143	0.4	0.538	0.727	0.824	0.906	0.980	1.0

Table 4: Triaxialities applied for FE simulations and values of corresponding model parameter η.

A total number of 456 FE calculations were carried out and listed in Tab. 5, with above-mentioned triaxial stress states, crystallographic orientations and porosities. The loading conditions are characterized by η_2 and η_3. Four cases were considered successively: $\eta_2 = \eta_3$, $\eta_2 = 0.4, \eta_2 = 0.727, \eta_2 = 1$. In each case, 10 values of η_3 were applied. The porosity $f = 0.01$ was first considered for 8 crystallographic orientations. Four more porosities $f = 0.005, 0.02, 0.05$ and 0.1 were considered, with 3 crystallographic orientations $[001], [111]$ and $[-125]$, and again 10 loading conditions. Additional tests are necessary to check the effect of porosity along other crystallographic orientations $[011]$ and $[210]$, for porosities $f = 0.005$ and 0.02.

The details of these simulations results will be presented and discussed in the next section. The model parameters α, q_2 and q_1 have been identified by minimizing (Levenberg-Marquardt method) the quadratic difference between model results and FE unit cell simulation results. Optimized values are given in Tab. 6. Comparison of these two sets of data after identification is shown in Fig. 3. The maximum error is always less than 10% and much smaller in many cases. Theoretical values for α, q_1 and q_2 are equal to 1 (see Eq. 6). The calibrated value for q_1 is close to 1.5 which is in agreement with the literature in the case of an isotropic von Mises matrix (see e.g. (Faleskog et al., 1998, Gao et al., 1998)). In particular a value for q_1 equal to 1.5 is very often used. The calibrated value for α is significantly higher than the theoretical one. Note that α plays an important role at high porosities (i.e. 5% and 10%).

Test details	**Number of tests**	**Figures**
8 orientations $f = 0.01 \times (4 \times 10$ FE calculations-3 redundant tests)	$8 \times (4 \times 10 - 3) = 296$	4-14
4 porosities $\times$ 3 orientations $\times 10$ FE calculations	$4 \times 3 \times 10 = 120$	16
$f = 0.005, f = 0.02, \times$ 2 orientations $[110]$ and $[210]$ $\times 10$ FE calculations	$2 \times 2 \times 10 = 40$	none[1]

[1] used only for parameter identification

Table 5: List of all the performed unit cell FE calculations.

α	q_1	q_2
6.456	1.471	1.325

Table 6: Adjusted values of model parameters.

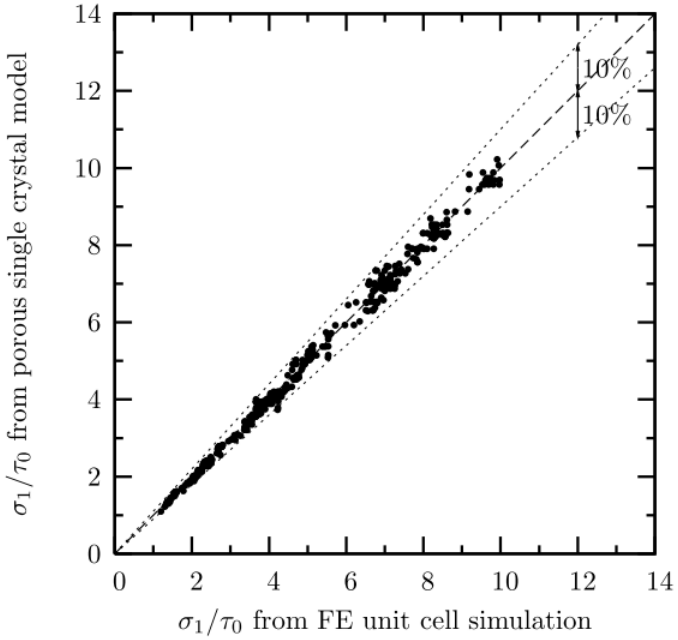

Figure 3: Identification results showing comparison points between FE unit cell simulations and effective single crystal model predictions. They are contained in a 10% error cone.

4. Results and discussions

In this section, the model predictions and unit cell analyses are compared for specific cases in order to examine the effect of crystallographic orientation and porosity on the resulting yield surface. Note that, for the sake of a nearly perfectly plastic behaviour used in FE simulations, the limit surfaces obtained from limit analyses could be considered as a good estimation of the yield surfaces. Therefore, it was assumed that the limit surface is identical to the yield surface so that in this section the "yield surface" term would be used to describe these two material properties.

4.1. Representation of the yield surface

The overall yield surface results, as in the case of a non porous single crystal, from the intersections of the yield surfaces (12 in the present case) for each individual slip system. It is therefore not possible to represent the macroscopic yield surface by expressing the von Mises stress as a function of the mean stress (i.e. $\sigma_{eq} = g\left(\sigma_m\right)$) as in the case of the Gurson model. In the following, the yield surface will be represented by plotting (3D plot) the macroscopic stress along the main loading direction **1** normalized by the CRSS, as a function of secondary loading parameters η_2 and η_3:

$$\sigma_1/\tau_0 = g(\eta_2, \eta_3) \tag{22}$$

In the case of axisymmetric loading (i.e. $\eta_2 = \eta_3 = \eta$), this normalized macroscopic stress is simply expressed as a function of η (2D plot) as:

$$\sigma_1/\tau_0 = g(\eta) \tag{23}$$

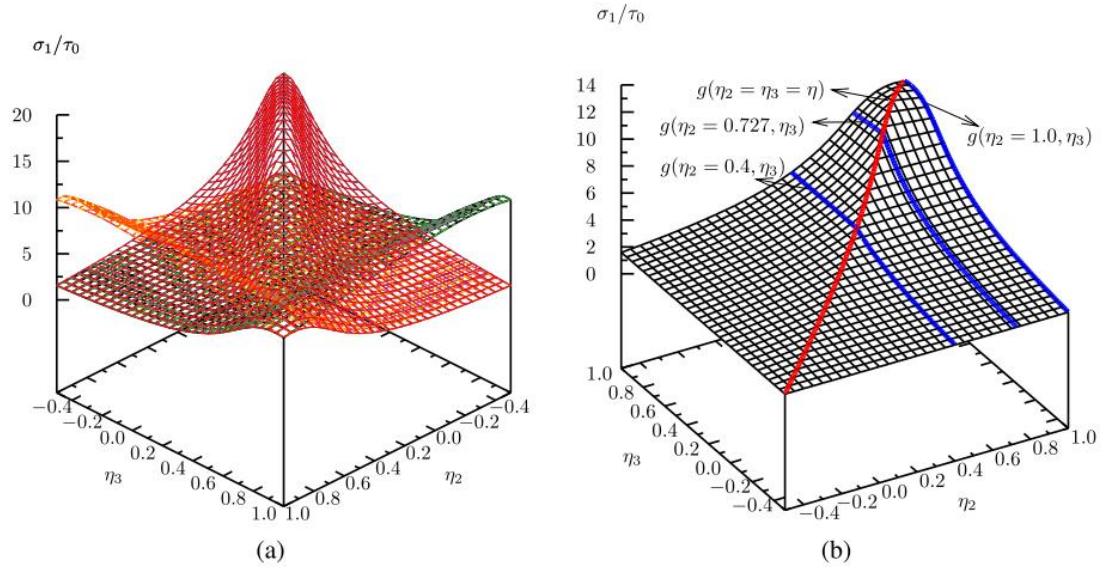

Figure 4: 3D yield surfaces for $[100] - [010] - [001]$ triaxial loading direction, with $f = 0.01$. (a) Yield surfaces for each of the 12 slip systems; (b) Yield surface for the porous single crystal.

4.2. Results for [100]–[010]–[001] *triaxial loading*

In this section, the three triaxial loading directions (**1**, **2** and **3**) coincide with the $\langle 100 \rangle$ directions of the single crystal. The porosity is equal to 1%. The resulting theroretical 12 yield surfaces (Eq. 8) for all slip systems are plotted in Fig. 4a while Fig. 4b shows the overall yield surface resulting from the intersection of the individual yield surfaces. In that particular loading case, it is important to recall that the $\langle 100 \rangle$ loading direction family leads to the same projection of the stress vector on the four slip planes of a FCC cystal (see Tab. 1). For this symmetry reason, only three distinct groups of curves are obtained, which correspond to the three slip systems on each slip plane (see Fig. 4a). In particular, the yield surface of the single crystal is symmetric with respect to the $\eta_2 = \eta_3$ line. Four special loading cases to be closely investigated in the following are indicated by colored lines (red and blue lines) in Fig. 4b: (i) $\eta_2 = \eta_3 = \eta$, (ii) $\eta_2 = 0.4$, (iii) $\eta_2 = 0.727$ and (iv) $\eta_2 = 1$. Model results Eq. (8) are now compared to unit cell simulation results.

Results for the $\eta_2 = \eta_3$ case are compared in Fig. 5a. In that particular case, the resulting yield surface is differentiable. This corresponds to the fact that the same slip systems are activated for all loading conditions. For this highly symmetric case, two of the three slip systems of each slip plane

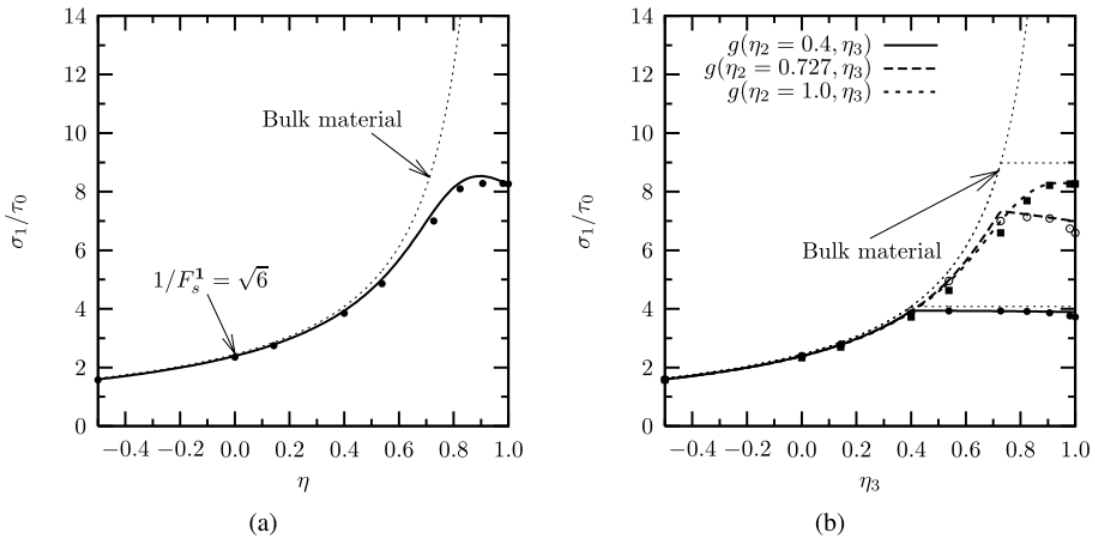

Figure 5: Yield surfaces for $[100] - [010] - [001]$ triaxial loading direction, with $f = 0.01$. (a) Yield surface for the porous single crystal, with $\eta_2 = \eta_3 = \eta$ (*i.e.* red curve in Fig. 4b). (b) Yield surfaces for the porous single crystal, with η_2 respectively fixed to 0.4, 0.727 and 1.0 (*i.e.* blue curves in Fig. 4b). Thick continuous and dashed lines correspond to the yield surfaces for the proposed model. Symbols correspond to 3D unit cell FE analyses. Thin dashed lines correspond to the bulk material (non porous single crystal) obtained from the proposed model for each studied case.

play the same role and are consequently active (in total eight slip systems are active). For the same reason, similar results are also obtained for the $\eta_2 = 1$ case (i.e. $\sigma_1 = \sigma_2$) in Fig. 5b, but the active slip systems are different from that of the previous case. However, in cases with η_2 fixed to 0.4 or 0.727 (Fig. 5b), two regimes are observed on the yield surface. In the case where $\eta_2 = 0.4$ (resp. $\eta_2 = 0.727$), only one slip system is active on each slip plane for η_3 between -0.5 and 0.4 (resp. 0.727). For η_3 above 0.4 (resp. 0.727), the active slip systems are replaced by different ones so that the resulting yield surface presents a discontinuous derivative at $\eta_3 = 0.4$ (resp. $\eta_2 = 0.727$). These evolutions are due to the behaviour of the matrix material only ; one can note that similar trends are observed for the non-porous single crystal (called bulk material in the figures, see the thin dashed lines in Fig. 5).

In all these cases, the proposed model accurately captures the FE simulations over the whole range of investigated stress triaxialities. Note that due to the low porosity level (1%), results obtained for the porous crystal and the bulk material remain close except for high stress triaxialities. In particular $\sigma_1 \to \infty$ when $\eta_2 \to 1$ and $\eta_3 \to 1$ for the bulk material whereas σ_1 keeps finite values for the porous single crystal. On the other hand for pure tensile loading ($\eta_2 = \eta_3 = 0$), both model and simulation are close to the theoretical value for the bulk single crystal: $\sigma_1/\tau_0 \approx 1/F_s^1 = \sqrt{6}$

where $F_s^{\mathbf{1}}$ is the Schmid factor for $[100]$ loading.

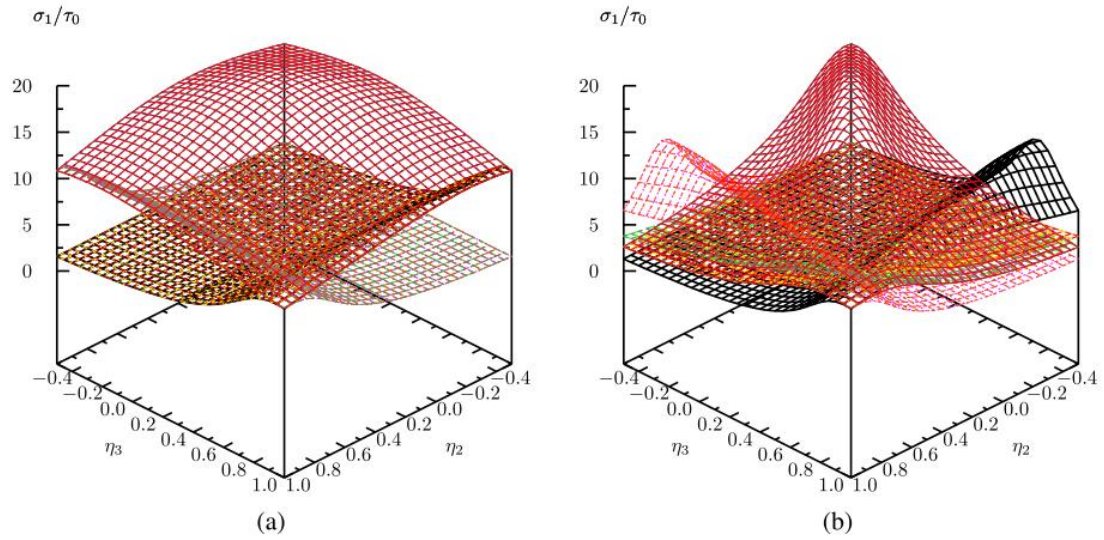

Figure 6: 3D yield surfaces for each of the 12 slip systems, with $f = 0.01$: (a) for $[100] - [01\overline{1}] - [011]$ triaxial loading direction; (b) for $[100] - [02\overline{1}] - [012]$ triaxial loading direction.

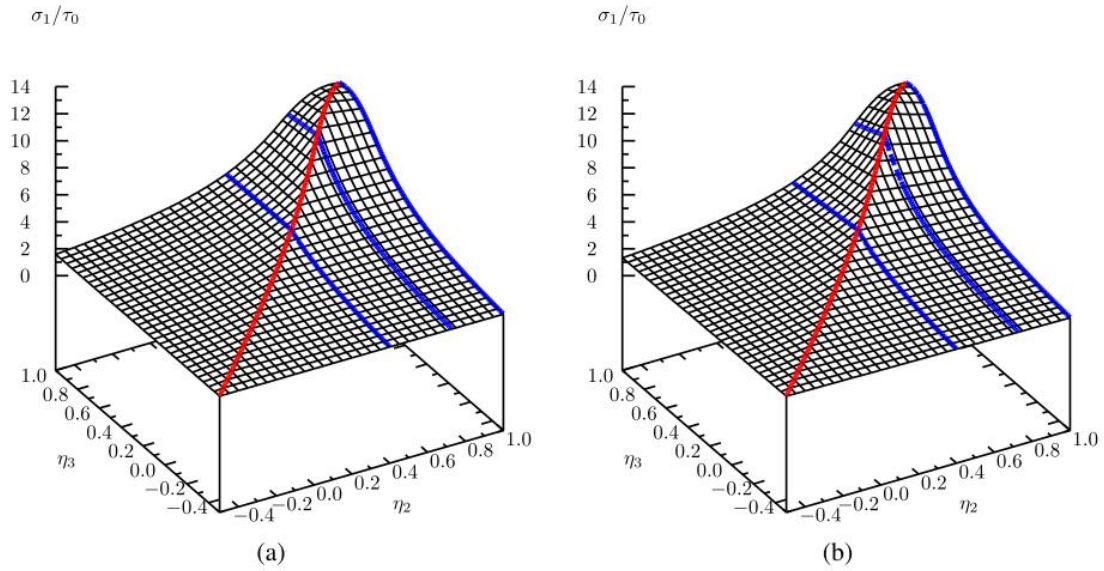

Figure 7: Yield surfaces for the porous single crystal, with $f = 0.01$: (a) for $[100] - [01\overline{1}] - [011]$ triaxial loading direction; (b) for $[100] - [02\overline{1}] - [012]$ triaxial loading direction.

4.3. Effect of secondary loading direction: $[100] - [0ij] - [0\overline{j}i]$

The effect of the secondary loading direction on the yield surface of the porous single crystal is investigated for a fixed main loading direction $\mathbf{1} = [100]$. The secondary loading direction **3** is

set to $[011]$ or to $[012]$. The yield surfaces for each effective slip system of the porous single crystal are illustrated respectively in Fig. 6a and Fig. 6b for these two cases. In the first case ($[100] - [01\overline{1}] - [011]$), just like in the reference case ([100]–[010]–[001]), the loading direction family $\langle 011 \rangle$ leads to the same Schmid factor for every activated slip system while for the other non-activated slip systems the Schmid factor is equal to zero. Moreover, the Schmid factors for $\langle 100 \rangle$ and $\langle 110 \rangle$ loading direction families have the same value ($F_s = \sqrt{6}/6$). For these reasons, only 3 groups of yield surfaces can be identified, and the yield surface of the overall porous single crystal (see Fig. 7a) presents exactly the same surface as in the reference case. However non-activated slip systems lead to different yield surfaces (compare Figs. 4a and 6a) so that the post-yield behaviour could be different in the case where the single crystal exhibits work-hardening.

In the second case ($[100] - [02\overline{1}] - [012]$), since the secondary loading direction does not lead to the same Schmid factor for every slip system, more numerous distinct yield surfaces are observed in Fig. 6b, and the yield surface for the porous single crystal in this case (Fig. 7b) is slightly different from the previous one.

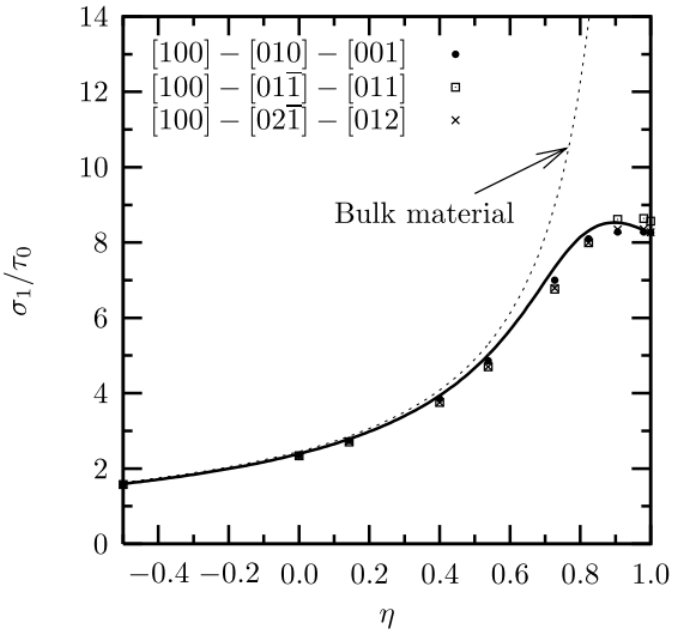

Figure 8: Yield surfaces for [100] main loading direction, in the case with $\eta_2 = \eta_3 = \eta$, for various secondary loading directions, $f = 0.01$.

Fig. 8 shows the yield surface predicted by the proposed model with corresponding data points calculated by FE method for $\eta_2 = \eta_3 = \eta$, for the same main loading direction $[100]$ and different secondary loading directions. As shown from Eq. 21, the secondary loading directions do not affect the predicted yield surface in this particular diagonal case. In the case explored by Figs. 9a and 9b, with fixed values for η_2, the yield surfaces are slightly different while the proposed model is able to

capture the FE simulation data with a good accuracy.

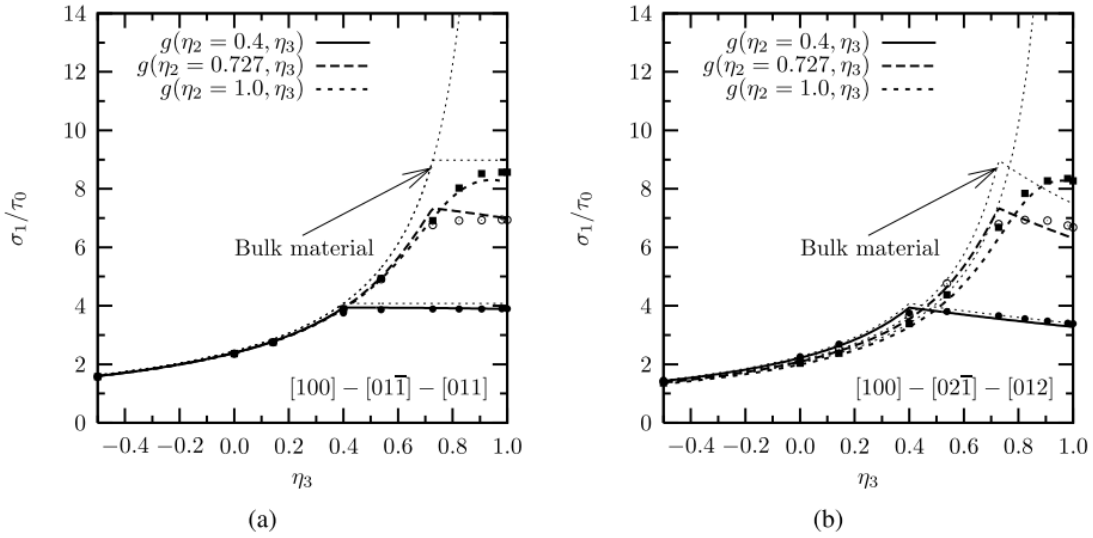

Figure 9: Yield surfaces for the porous single crystal, in the cases of η_2 fixed at 0.4, 0.727 and 1.0, with $f = 0.01$: (a) for $[100] - [01\overline{1}] - [011]$ triaxial loading direction; (b) for $[100] - [02\overline{1}] - [012]$ triaxial loading direction.

4.4. Effect of main loading direction

The effect of the main loading direction (**1**) is investigated in this section. Comparisons between results obtained by the proposed model and by FE unit cell simulations are shown for the following orientations $[110]$ (see Fig. 10), $[111]$ (see Fig. 11), $[210]$ (see Fig. 12) and finally $[\overline{1}25]$ (see Fig. 13). In this last case, the effect of the secondary loading direction (**3**) is also studied.

Yield surfaces predicted by the model for main loading directions taken equal to $[110]$, $[111]$ or $[210]$ significantly differ (see Figs. 10b, 11b and 12b). In comparison to the $\mathbf{1} = [100]$ case, yield surfaces are no longer symmetric with respect to the $\eta_2 = \eta_3$ line. As previously noted, the sharp slope changes on the yield surfaces correspond to a change in the active slip systems. These trends are directly due to the crystallographic nature of the matrix material. Due to the low porosity, the difference between the yield surface of the bulk material (see Figs. 10c/10d, 11c/11d and 12c/12d) and that of the porous material is only significant at high stress triaxiality levels. In all cases, the model prediction and the FE unit cell results are in very good agreement (see Figs. 10c/10d, 11c/11d and 12c/12d, model: lines, FE results: symbols)

All cases presented above exhibit some degree of symmetry so that several individual slip systems may have the same yield surface. In order to check the validity of the proposed model in cases where loading has little or no symmetry with respect to the crystallographic orientation, main loading

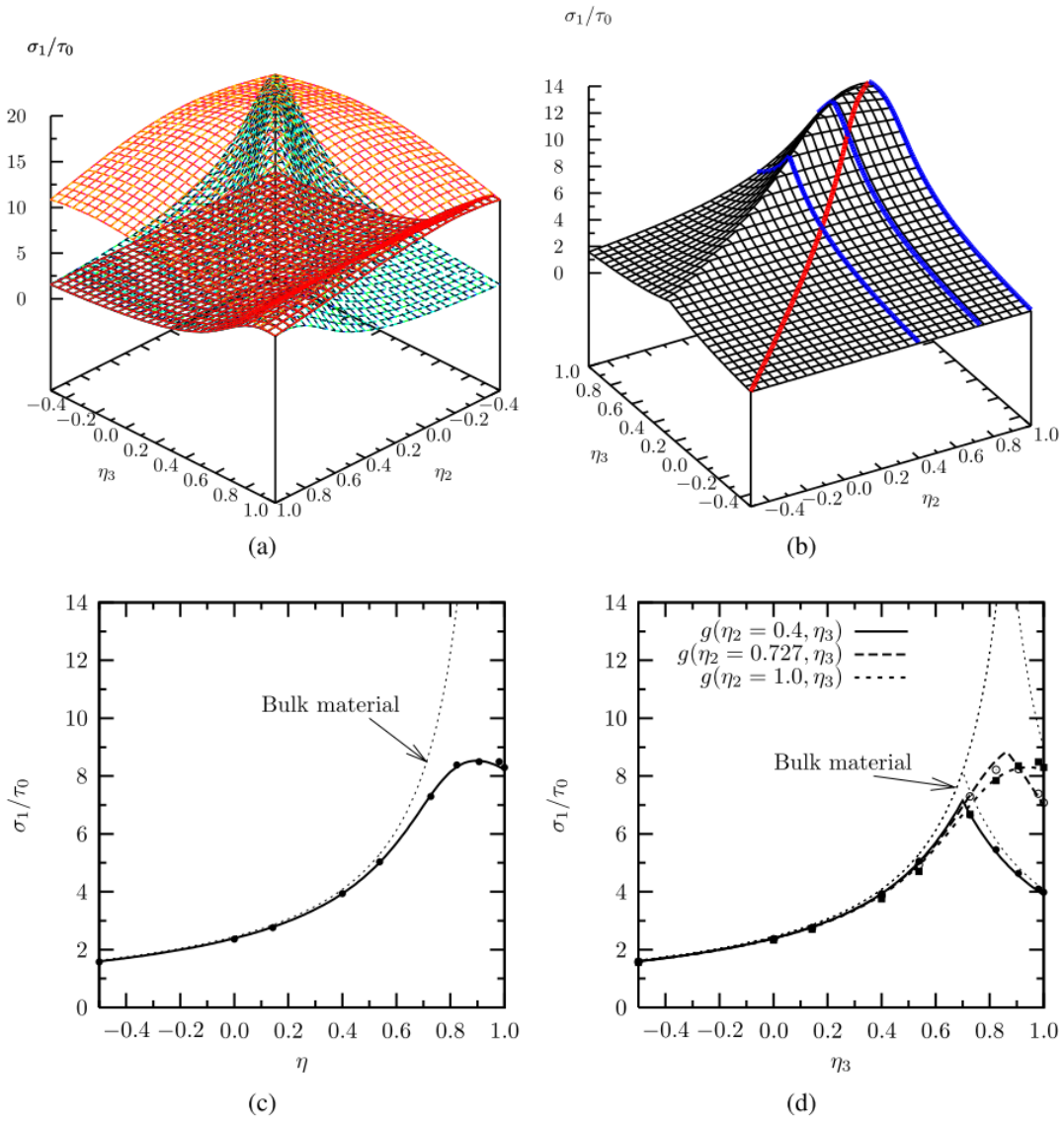

Figure 10: Yield surfaces for $[110] - [\bar{1}10] - [001]$ triaxial loading direction, with $f = 0.01$. (a) 3D yield surfaces for all 12 slip systems; (b) 3D yield surface for the porous single crystal. (c) Yield surface for the porous single crystal, with $\eta_2 = \eta_3 = \eta$; (d) Yield surfaces for the porous single crystal, with η_2 fixed at 0.4, 0.727 and 1.0.

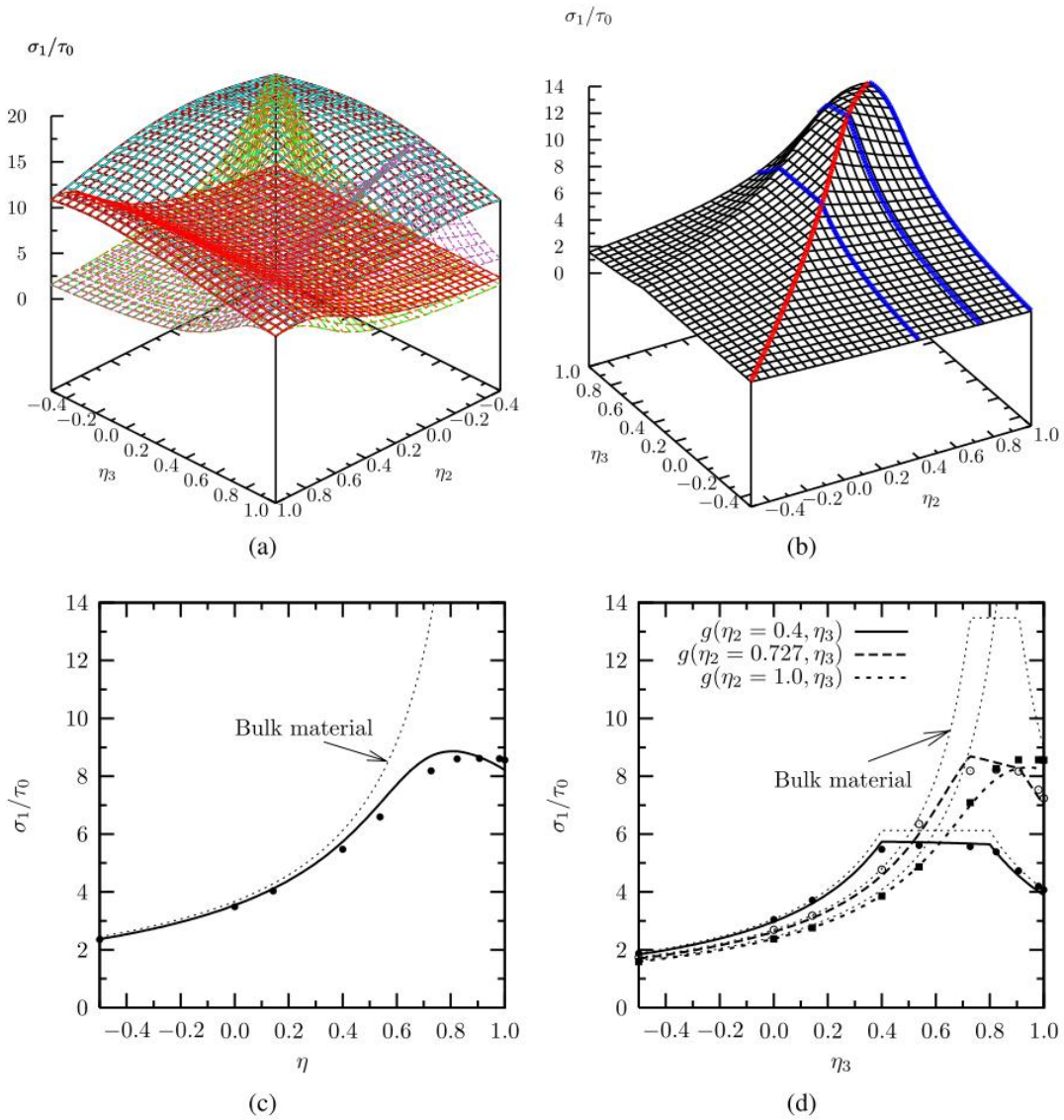

Figure 11: Yield surfaces for $[111] - [\bar{2}11] - [0\bar{1}1]$ triaxial loading direction, with $f = 0.01$. (a) 3D yield surfaces for all 12 slip systems; (b) 3D yield surface for the porous single crystal. (c) Yield surface for the porous single crystal, with $\eta_2 = \eta_3 = \eta$; (d) Yield surface for the porous single crystal, with η_2 fixed at 0.4, 0.727 and 1.0.

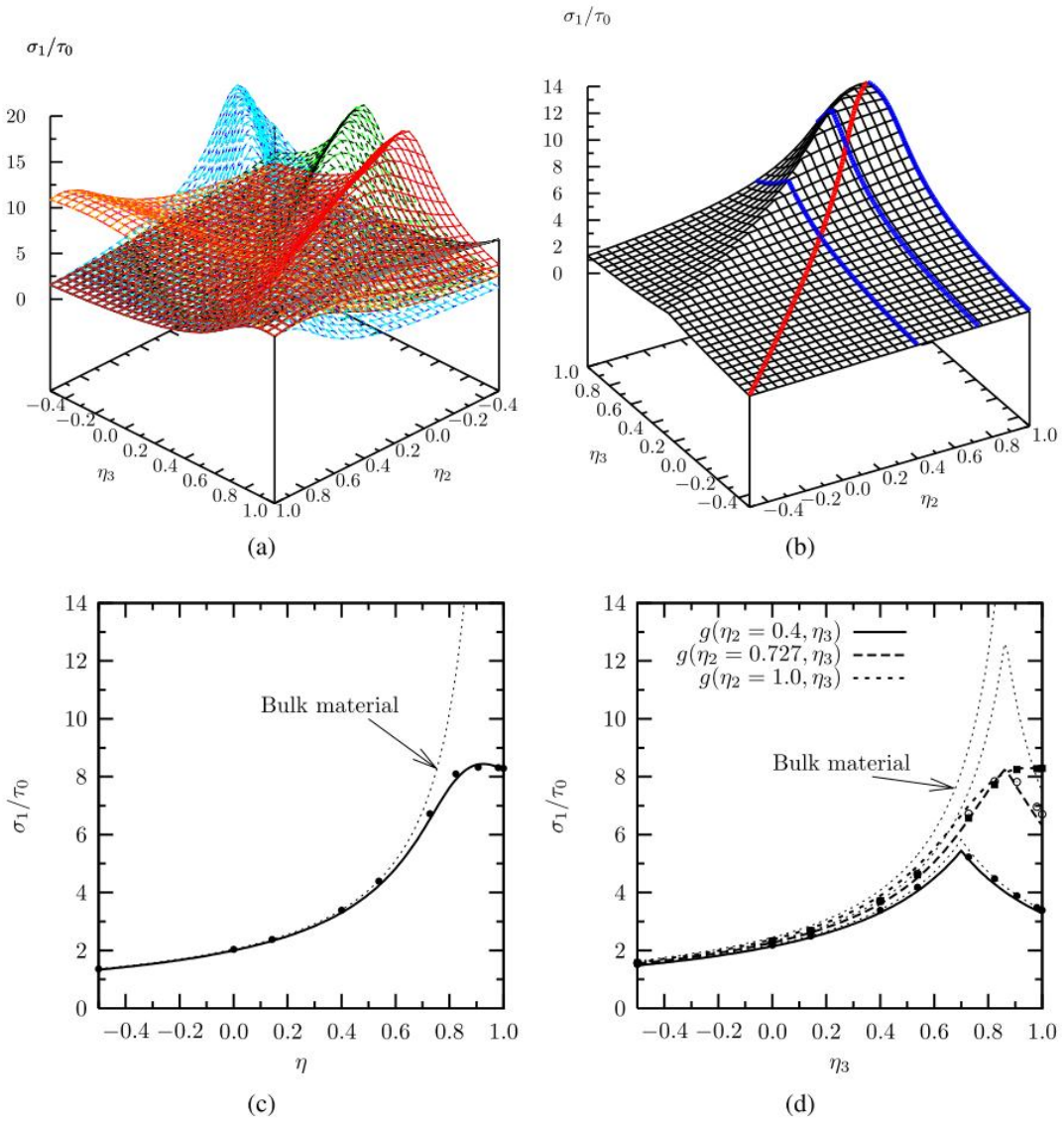

Figure 12: Yield surfaces for $[210] - [\bar{1}20] - [001]$ triaxial loading direction, with $f = 0.01$. (a) 3D yield surfaces for all 12 slip systems; (b) 3D yield surface for the porous single crystal. (c) Yield surface for the porous single crystal, with $\eta_2 = \eta_3 = \eta$; (d) Yield surface for the porous single crystal, with η_2 fixed at 0.4, 0.727 and 1.0.

along the $[\bar{1}25]$ crystal direction was investigated. For $\mathbf{3} = [210]$, 11 different yield surfaces for the slip systems are obtained whereas for $\mathbf{3} = [(29)25]$ all 12 yield surfaces differ. The resulting theoretical yield surfaces are plotted in Figs. 13 for both secondary loading directions. Comparisons with FE results are shown in Fig. 14a for the $\eta_2 = \eta_3$ case, in Fig. 14b for various fixed values for η_2 and $\mathbf{3} = [210]$ and Fig. 14c for various fixed values for η_2 and $\mathbf{3} = [(29)25]$. The agreement between the model and the simulation results is excellent. Note, in particular, that the differences between $\mathbf{3} = [210]$ and $\mathbf{3} = [(29)25]$ at high stress triaxialities are well reproduced by the model (Fig. 14b and Fig. 14c).

Yield surfaces in the particular case where $\eta_2 = \eta_3$ are compared in Fig. 15 for five different main loading directions. In that particular case results for $\mathbf{1} = [100]$ and $\mathbf{1} = [110]$ coincide as well as those for $\mathbf{1} = [210]$ and $\mathbf{1} = [\bar{1}25]$ as they share the same maximum Schmid factor. At low and moderate stress triaxialities the differences between the yield surfaces is controlled by the value of the Schmid factor for the bulk material. These differences tend to decrease at very high triaxiality levels. Under purely hydrostatic loads ($\eta \to 1$) the model predicts a unique yield stress σ_1 which is given by (solving Eq. 8 and Eq. 9 for $\tau_s = \sigma_{eq} = 0$ and $\sigma_m = \sigma_1$):

$$\frac{\sigma_1}{\tau_0} = \frac{1}{q_2}\sqrt{\frac{20}{3}}\text{arccosh}\left(\frac{1+(q_1 f)^2}{2q_1 f}\right) \tag{24}$$

This limit is well verified by the FE simualtions.

4.5. Effect of void volume fraction f

The results presented above were obtained for a fixed porosity level (1%). In this section, the model and the unit cell calculations are compared for porosities equal to 0.5%, 1%, 2%, 5% and 10%. For the sake of conciseness, the comparison is limited to the case where $\eta_2 = \eta_3$ for a main loading direction equal to $[100]$ (equivalent to $[110]$ for $\eta_2 = \eta_3$), $[111]$ or $[\bar{1}25]$ (equivalent to $[210]$ for $\eta_2 = \eta_3$). Results are shown in Fig. 16. Comparisons with results corresponding to the bulk material (thin dashed lines) are also presented. It is clearly observed that, for low triaxialities, the effect of porosity on the yield surface is rather limited so that yield surfaces for the voided materials are very close to the curve for the bulk material. Despite this moderate effect, FE simulations for these triaxiality and porosity ranges are needed to calibrate parameter α. The original model developed in Appendix A strongly underestimates the trends obtained using FE simulations with $\alpha = 1$ whereas the optimized value is much larger ($\alpha = 6.46$). At high triaxiality ratio, Eq. 24 appears to well represent FE simulations for the entire porosity range and all loading directions.

4.6. Field of plastic slip activation around the hole

The unit cell computations do no provide only results at the macroscopic scale but also fields of plastic deformation around the hole that bring information about the deformation modes of a hole

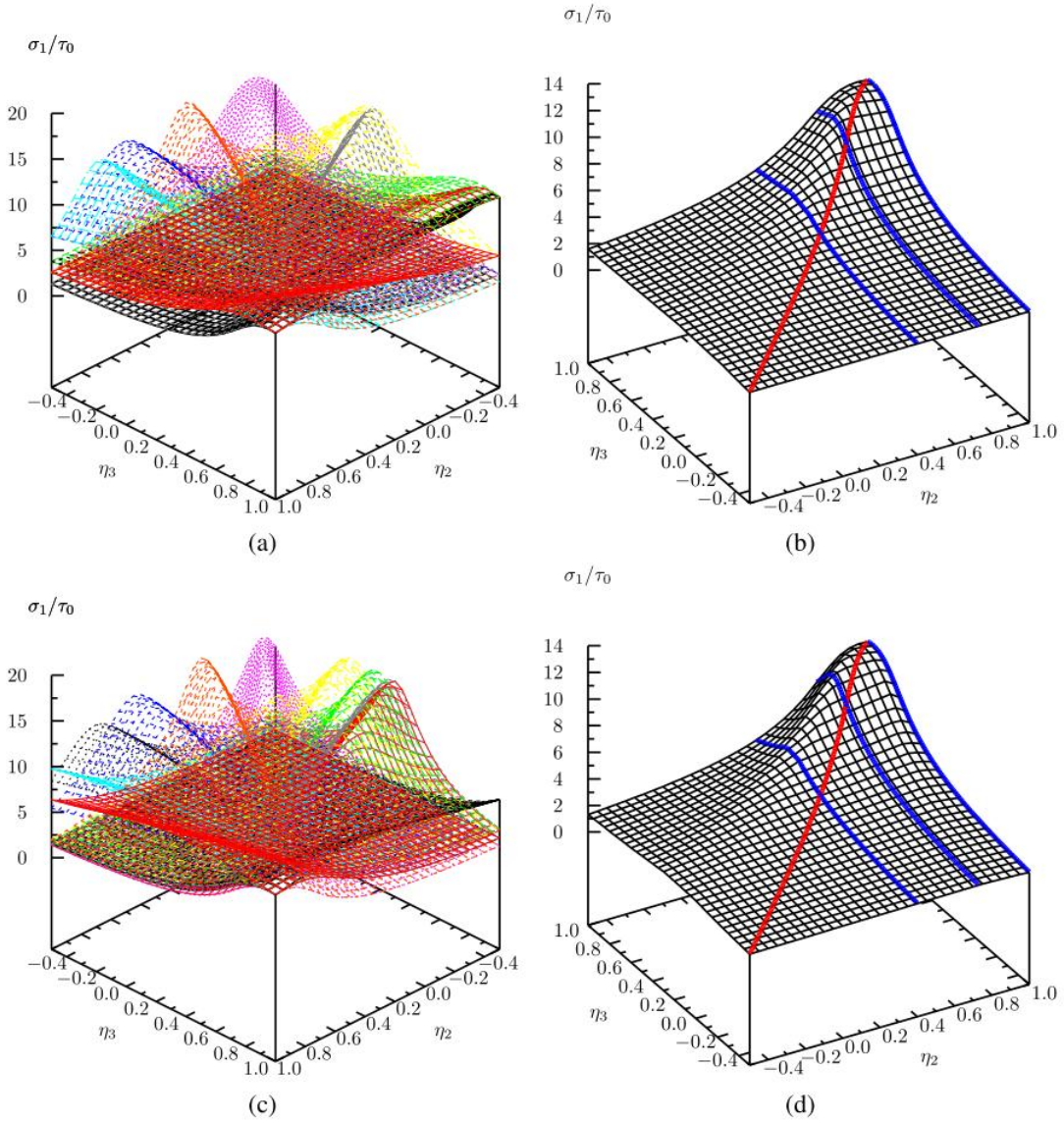

Figure 13: $[\bar{1}25]$ loading: (a) 3D yield surfaces for each slip system for $\mathbf{3} = [210]$, (b) 3D yield surface for the porous single crystal for $\mathbf{3} = [210]$, (c) 3D yield surfaces for each slip system for $\mathbf{3} = [(29)25]$, (d) 3D yield surface for the porous single crystal for $\mathbf{3} = [(29)25]$

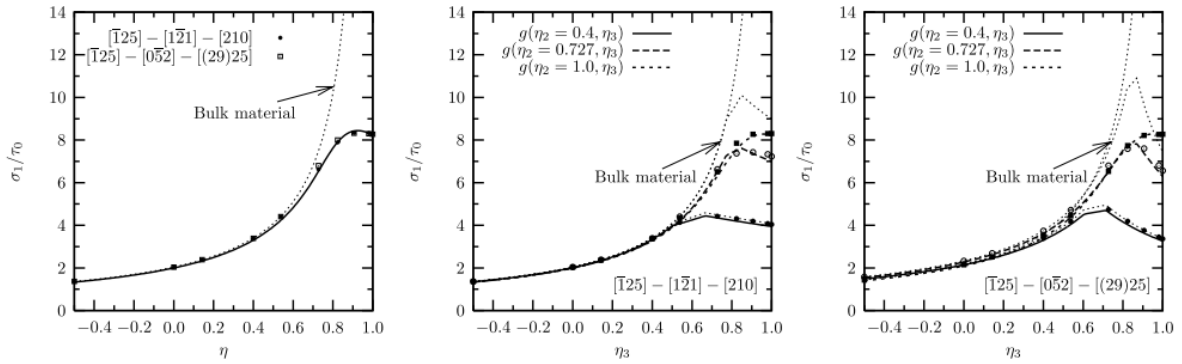

(a) (b) (c)

Figure 14: Yield surfaces for the porous single crystal for $[\bar{1}25]$ loading, $f = 0.01$: (a) $\eta_2 = \eta_3 = \eta$ for $\mathbf{3} = [210]$ and $\mathbf{3} = [(29)25]$, (b) for $\mathbf{3} = [210]$ and $\eta_2 = 0.4$, 0.727 and 1, (c) for $\mathbf{3} = [(29)25]$ and $\eta_2 = 0.4$, 0.727 and 1.

in a single crystal. The impact of crystallography on the shape evolution of a hole in a single crystal matrix during growth was studied by Yerra et al. (2010) within the framework of finite deformation crystal plasticity. Since the limit analysis provided in the present work is limited to small strain, the shape changes are not illustrated here. Instead, maps are now provided showing the activation of slip systems around the hole depending on crystal orientation and prescribed stress triaxiality. For that purpose, the total cumulative slip γ_{cum} is defined as the sum of all the cumulative slip variables γ^s:

$$\gamma_{cum} = \sum_{s=1}^{12} \gamma^s \tag{25}$$

The field of total cumulative slip is illustrated in Fig. 17 for three different crystal orientations and three triaxiality levels for fixed values of porosity (1%) and mean strain. The pictures show middle cross–sections of the unit cell in the **1–2** plane, where 1 and 2 refer to the two first crystal directions indicated in the orientation of the cell. The inhomogeneity of plastic slip appears clearly in these maps with an obvious symmetry of the deformation patterns for the $[100]-[010]-[001]$ orientation, in contrast to the two other ones where symmetry is broken.

Figure 18 shows the activation of the 12 slip systems around the hole in the case of an imposed triaxiality of 1.5, for the specific orientation $[111]-[\bar{2}11]-[0\bar{1}1]$ with a given overall strain level. It turns out that all the slip systems are activated at some places, mainly around the North and South poles on the figure where multiple slip is observed. The fact that the twelve slip systems are activated at some place in the unit cell in contrast to the corresponding bulk single crystal is probably one reason why the von Mises equivalent stress must be introduced in the proposed yield function (Eq. 8) in addition to the resolved shear stress.

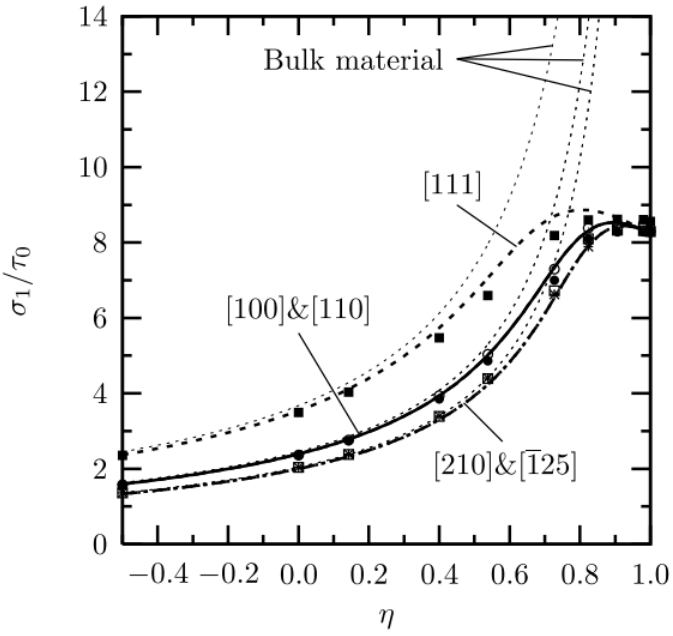

Figure 15: Effect of the main loading direction **1** on the yield surface for the porous single crystal, in the case with $\eta_2 = \eta_3 = \eta$, $f = 0.01$.

5. Conclusion

The original contribution of the present work to the modeling of ductile fracture in single crystals is to provide a yield function in closed form for porous single crystals and to validate it by means of systematic unit cell computations. It is theoretically motivated using a variational micromechanical approach. It is formulated as the combination of N yield criteria, N being the number of potential slip systems in the single crystal matrix, based on the definition of a new effective equivalent stress measure for each slip system. This equivalent stress measure incorporates in a nonlinear way the resolved shear stress on the considered slip system and the equivalent von Mises and mean stresses. To better match an exponential dependence on the mean stress (which is well recognized for rate-independent materials), this yield function was phenomenologically extended following a procedure similar to the GTN extension of Gurson's model (Tvergaard and Needleman (1984) and Leblond et al. (1994)). The extension introduces three adjustable parameters (q_1, q_2 and α). Unit cell simulations were used to fit these parameters in the case of a FCC single crystal. Various stress triaxiality ratios, main loading directions and porosity levels were considered for the unit cell simulations. In all cases, the model was able to capture the results of the calculations with a very good accuracy, including the effects of main loading direction, of secondary loading direction and of porosity.

Further work will include the analysis of the plastic flow rule associated with the proposed yield

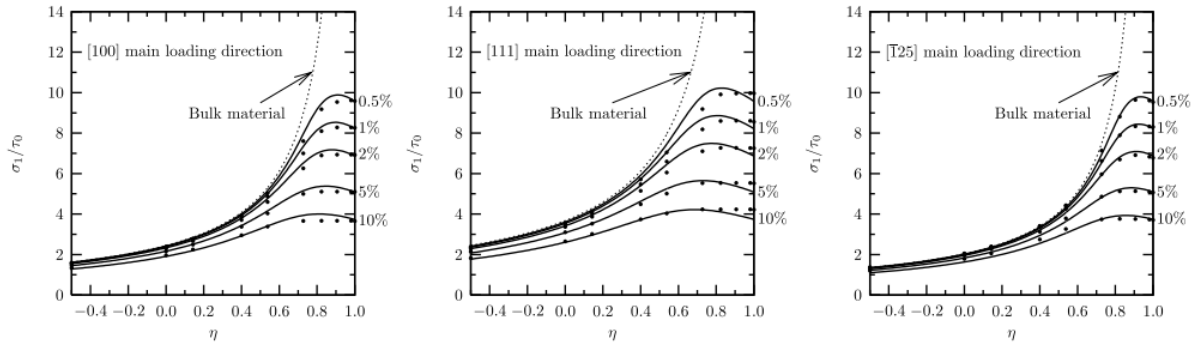

(a) (b) (c)

Figure 16: Effect of porosity from 0.5% to 10% for various main loading directions, with $\eta_2 = \eta_3 = \eta$: (a) $[100]$ main loading direction; (b) $[111]$ main loading direction; (c) $[\bar{1}25]$ main loading direction.

function. In particular, the validity of the normality rule Eq. 10 will be tested for this new yield criterion. In addition, the porosity growth rate ($\dot{f} = (1-f)\text{trace}(\underline{\dot{\varepsilon}}_p)$) will be investigated by comparing the results of the model and unit cell simulations. It is well–known that crystallographic aspects of plastic deformation around holes strongly affect their growth rate, for example in H.C.P. metals, see Crépin et al. (1996). The proposed yield function will then be used to develop a set of constitutive equations for the porous single crystal including self and cross-hardening within a finite strain framework. A first application of this model will be the evaluation of the fracture toughness properties in presence of swelling in irradiated stainless steels.

Appendix A. Development of a model for voided viscous single crystals

In this section a model is developed for viscous single crystals containing spherical voids. The single crystal is assumed to have a nonlinear viscous behaviour with N slip systems. Following DeBotton and Ponte Castañeda (1995) each slip system is associated to a slip potential function ϕ_s defined as:

$$\phi_s = \frac{\dot{\gamma}_0 \tau_0}{n+1} \left| \frac{\tau_s}{\tau_0} \right|^{n+1} \tag{A.1}$$

where $\dot{\gamma}_0 (> 0)$ and $\tau_0 (> 0)$, respectively, are the reference slip rate and the reference flow stress of slip system s. The creep exponent is denoted by n and τ^s is the resolved shear stress on the slip system *s*, given by:

$$\tau_s = \underline{\sigma} : \underline{m}_s \tag{A.2}$$

where $\underline{m}_s$ is the orientation tensor defined by Eq. 1. The overall stress potential of the single crystal is the sum of the potentials for all slip systems:

$$\Phi(\underline{\sigma}) = \sum_{s=1}^{N} \phi_s(\tau_s) \tag{A.3}$$

As defined in Eq. A.1, ϕ_s is a power law function which is strictly convex.

Based on the work by DeBotton and Ponte Castañeda (1995), a stress potential for a linear comparison single crystal is introduced as:

$$\Phi_L(\underline{\sigma}) = \frac{1}{2}\underline{\sigma} : \mathbb{M}^\chi : \underline{\sigma} = \sum_{s=1}^{N} \alpha_s \tau_s^2 \tag{A.4}$$

where α_s denotes the slip system compliance. The fourth-order compliance tensor is written as:

$$\mathbb{M}^\chi = 2\sum_{s=1}^{N} \alpha_s \underline{m}_s \otimes \underline{m}_s = 2\sum_{s=1}^{N} \alpha_s \mathbb{R}_s \tag{A.5}$$

Then, according to DeBotton and Ponte Castañeda (1995) dual potentials are defined as:

$$\phi_s(\tau_s) = \max_{\alpha_s \geqslant 0}\{\alpha_s \tau_s^2 - V_s(\alpha_s)\} \tag{A.6}$$

$$V_s(\alpha_s) = \max_{\tau_s \geqslant 0}\{\alpha_s \tau_s^2 - \phi_s(\tau_s)\} \tag{A.7}$$

Using Eq. A.1 together with Eq. A.7, by taking account of the convexity of the viscous potential with $n > 1$, the function V_s can be explicitly expressed as:

$$V_s(\alpha_s) = \frac{n-1}{n+1}\frac{\dot{\gamma}_0 \tau_0}{2}\left(\frac{2\tau_0 \alpha_s}{\dot{\gamma}_0}\right)^{\frac{n+1}{n-1}} \tag{A.8}$$

Based on this constitutive model for the single crystal, the porous single crystal can be further described introducing a variational characterization as proposed in (Ponte Castañeda, 1991, 1992a). The effective stress potential for the "composite" (i.e. single crystal + voids) is derived from the theorem of minimum complementary potential energy, by the following relation:

$$\overline{\Phi}(\underline{\Sigma}) = \min_{\underline{\sigma}(\vec{x}) \in \boldsymbol{S}} \int_\Omega \Phi(\underline{\sigma}(\vec{x}))d\Omega \tag{A.9}$$

with Ω being the representative volume element containing voids and the metallic matrix, $\underline{\Sigma}$ the macroscopic stress tensor defined as the average over the total volume $\underline{\Sigma} = \langle \underline{\sigma}(\vec{x}) \rangle_\Omega$, and $\boldsymbol{S}$ the set of Statically Admissible (S.A.) stress fields with a homogeneous stress boundary condition on the outer boundary $\partial\Omega$ of Ω: $\underline{\sigma}(\vec{x})$ S.A. $\Longleftrightarrow \underline{\sigma} \in \boldsymbol{S}$ with $\boldsymbol{S} = \{\mathrm{div}(\underline{\sigma}) = \vec{0}$ in Ω and $\underline{\sigma}.\vec{n} = \underline{\Sigma}.\vec{n}$ on $\partial\Omega\}$ where $\vec{n}$ is the outer normal to the boundary, $\partial\Omega$, of Ω.

Following Ponte Castañeda (1992b) and Ponte Castañeda and Zaidman (1996), the effective potential can be estimated as:

$$\overline{\Phi}(\underline{\Sigma}) \geqslant \max_{\{\alpha_r \geqslant 0\}_{r=1,N}} \left(\overline{\Phi}_L(\underline{\Sigma}) - (1-f) \sum_{s=1}^{N} V_s(\alpha_s) \right) \tag{A.10}$$

where $\overline{\Phi}_L(\underline{\Sigma})$ denotes any estimate of the potential of the linear composite. $\overline{\Phi}_L$ can be expressed as:

$$\overline{\Phi}_L(\underline{\Sigma}) = \frac{1}{2} \underline{\Sigma} : \overline{\mathbb{M}} : \underline{\Sigma} \tag{A.11}$$

where $\overline{\mathbb{M}}$ is an estimate of the effective viscous compliance fourth order tensor of the "composite". In Eq. A.10 it has been assumed that the slip system compliance α_s can be considered as identical for each slip system of the single crystal and independent of the position in Ω. Furthermore, the $(1-f)$ factor accounts for the fact that only a fraction of the composite corresponds to the single crystal. The remainder (i.e. f) corresponds to voids for which the V function is equal to zero.

In the following, Eq. A.10 will be regarded as an equality in order to obtain an estimate of the potential of the composite (Ponte Castañeda and Zaidman, 1996). To proceed it is also necessary to select a proper estimate of the effective stress potential of the linear comparison single crystal ($\overline{\Phi}_L$). In the following a Hashin-Shtrikman lower bound will be used. In that case the effective viscous compliance tensor $\overline{\mathbb{M}}$ (referred to as $\overline{\mathbb{M}}^{\mathrm{HS}-}$) is given by the following equation (DeBotton and Ponte Castañeda, 1995):

$$\left[\overline{\mathbb{M}}^{\mathrm{HS}-} + \mathbb{M}^*\right]^{-1} = (1-f)\left[\mathbb{M}^{\chi} + \mathbb{M}^*\right]^{-1} + f\left[\mathbb{M}^{\mathrm{v}} + \mathbb{M}^*\right]^{-1} \tag{A.12}$$

where $\mathbb{M}^{\mathrm{v}}$ is the compliance tensor of the voids. $\mathbb{M}^*$ is the inverse of the influence tensor of Hill for a spherical void. As the bulk and shear moduli of the void are equal to zero, Eq. A.12 leads to:

$$\overline{\mathbb{M}}^{\mathrm{HS}-} = \frac{1}{1-f}\mathbb{M}^{\chi} + \frac{f}{1-f}\mathbb{M}^* \tag{A.13}$$

The inverse of the influence tensor of Hill can easily be computed in the case of an isotropic compliance matrix which is expressed as [2]:

$$\mathbb{M}_0 = \frac{1}{3\kappa_0}\mathbb{J} + \frac{1}{2\mu_0}\mathbb{K} \tag{A.14}$$

In the case where the matrix material can be considered as incompressible (i.e. $\kappa_0 \to \infty$), the tensor $\mathbb{M}^*$ is found to be:

$$\mathbb{M}^* = \frac{1}{4\mu_0}\mathbb{J} + \frac{1}{3\mu_0}\mathbb{K} \equiv \frac{1}{3\kappa^*}\mathbb{J} + \frac{1}{2\mu^*}\mathbb{K} \tag{A.15}$$

[2] $\mathbb{J}$ and $\mathbb{K}$ are fourth order tensors such that: $\mathbb{J} : \underline{a} = \frac{1}{3} a_{kk} \underline{1}$ and $\mathbb{K} : \underline{a} = \underline{a} - \frac{1}{3} a_{kk} \underline{1}$ (deviator of $\underline{a}$) for any second order tensor $\underline{a}$.

In the following $\mathbb{M}_0$ (defined by the shear modulus μ_0 only) will be used instead of $\mathbb{M}^\chi$ to compute $\mathbb{M}^*$, since no direct expression for $\mathbb{M}^*$ as a function of $\mathbb{M}^\chi$ is available. A suitable value for μ_0 must consequently be used. In that case the lower bound character of the model is lost. As a first approximation, it is assumed that the deviatoric projections of $\mathbb{M}^\chi$ and $\mathbb{M}_0$ are equal so that:

$$\mathbb{M}^\chi :: \mathbb{K} = \mathbb{M}_0 :: \mathbb{K} \tag{A.16}$$

Noting that $\mathbb{K} :: \mathbb{K} = 5$ and that $\mathbb{R}_s :: \mathbb{K} = \frac{1}{2}$, $\forall s$, one finally obtains from A.5 and A.14 :

$$\mu_0 = \frac{5}{2\sum_s \alpha_s} \tag{A.17}$$

Using relation A.13, the effective stress potential of the porous linear comparison single crystal can be approximated as:

$$\begin{aligned} \overline{\Phi}_L(\underline{\Sigma}) &= \frac{1}{2}\underline{\Sigma} : \overline{\mathbb{M}}^{\mathrm{HS}-} : \underline{\Sigma} = \frac{1}{2}\underline{\Sigma} : \left(\frac{1}{1-f}\mathbb{M}^\chi + \frac{f}{1-f}\mathbb{M}^*\right) : \underline{\Sigma} \\ &= \frac{1}{1-f}\left(\sum_s \alpha_s T_s^2 + f\overline{\Phi}^*(\underline{\Sigma})\right) \end{aligned} \tag{A.18}$$

where $T_s = \underline{\Sigma} : \underline{m}^s$ is the macroscopic resolved shear stress of the slip system s for the non-linear single crystal and $\overline{\Phi}^*(\underline{\Sigma})$ is derived from A.11 and A.15:

$$\overline{\Phi}^*(\underline{\Sigma}) = \frac{1}{2\kappa^*}\Sigma_m^2 + \frac{1}{6\mu^*}\Sigma_{eq}^2 \tag{A.19}$$

where Σ_m (resp. Σ_{eq}) is the mean stress (resp. von Mises stress) of the macroscopic stress tensor $\underline{\Sigma}$. Note that $\overline{\Phi}^*$ is expressed using isotropic invariants of $\underline{\Sigma}$ because $\mathbb{M}_0$ is assumed to be isotropic as a first approximation. Finally $\overline{\Phi}_L$ can be expressed as:

$$\overline{\Phi}_L(\underline{\Sigma}) = \frac{1}{1-f}\sum_{s=1}^{N}\left\{\alpha_s\left[T_s^2 + f\left(\frac{3}{20}\Sigma_m^2 + \frac{2}{45}\Sigma_{eq}^2\right)\right]\right\} \tag{A.20}$$

It follows that the estimate of the effective potential $\overline{\Phi}$ can be rewritten using A.10 and A.8 as:

$$\begin{aligned} \overline{\Phi}(\underline{\Sigma}) &= \max_{\{\alpha_r \geqslant 0\}_{r=1,N}}\left[\frac{1}{1-f}\sum_{s=1}^{N}\left(\alpha_s\left(T_s^2 + f\left(\frac{3}{20}\Sigma_m^2 + \frac{2}{45}\Sigma_{eq}^2\right)\right)\right)\right. \\ &\quad \left. -(1-f)\sum_{s=1}^{N}\frac{n-1}{n+1}\frac{\dot{\gamma}_0\tau_0}{2}\left(\frac{2\tau_0\alpha_s}{\dot{\gamma}_0}\right)^{\frac{n+1}{n-1}}\right] \end{aligned} \tag{A.21}$$

At this stage of the derivation it is convenient to introduce the following quantity:

$$T_s^* = \frac{1}{1-f}\left(T_s^2 + f\left(\frac{2}{45}\Sigma_{eq}^2 + \frac{3}{20}\Sigma_m^2\right)\right)^{\frac{1}{2}} \tag{A.22}$$

In order to maximize the right hand-side of Eq. A.21 one needs to solve the system of equations formed by the vanishing of the partial derivatives of the argument of the Max operator in (A.21) with respect to α_s, $\forall s$. This leads to:

$$\alpha_s = \frac{\dot{\gamma}_0}{2\tau_0}\left(\frac{T_s^*}{\tau_0}\right)^{n-1} \tag{A.23}$$

Introducing this solution into Eq. A.21 leads to the following expression for $\overline{\Phi}$:

$$\overline{\Phi}(\underline{\Sigma}) = (1-f)\sum_s \frac{\dot{\gamma}_0\tau_0}{n+1}\left|\frac{T_s^*}{\tau_0}\right|^{n+1} \equiv \sum_s \overline{\phi}_s(T_s^*) \tag{A.24}$$

Based on this equation, effective slip systems can be attributed to the homogenized porous single crystal whereby T_s^* can be interpreted as an effective scalar resolved stress acting on each slip system. Rate independent plasticity is obtained for $n \to +\infty$. The yield surface for each slip system is then expressed as: $T_s^* - \tau_0 = 0$.

References

Bandstra, J., Koss, D., 2008. On the influence of void clusters on void growth and coalescence during ductile failure. Acta Materialia 56, 4429–4439.

Benzerga, A., Besson, J., Pineau, A., 2004. Anisotropic ductile fracture: Part II: theory. Acta Metall. 52, 4639–4650.

Benzerga, A., Leblond, J., 2010. Ductile fracture by void growth to coalescence. Adv. Appl. Mech. 44, 169–305.

Benzerga, A. A., Besson, J., 2001. Plastic potentials for anisotropic porous solids. Eur. J. Mech./A 20 (3), 397 – 434.

Besson, J., 2010. Continuum models of ductile fracture: A review. Int. J. Damage Mech. 19 (1), 3–52.

Besson, J., Cailletaud, G., Chaboche, J.-L., Forest, S., Blétry, M., 2009. Non–Linear Mechanics of Materials. Series: Solid Mechanics and Its Applications, Vol. 167, Springer.

Besson, J., Foerch, R., 1998. Application of object-oriented programming techniques to the finite element method. Part I-General concepts. Revue Europenne des Elements Finis 7 (5), 535–566.

Besson, J., Steglich, D., Brocks, W., 2001. Modeling of crack growth in round bars and plane strain specimens. Int. J. Solids Structures 38 (46–47), 8259–8284.

Brocks, W., Sun, D. Z., Honig, A., 1995. Verification of the transferability of micromechanical parameters by cell model calculations with visco-plastic materials. Int. J. Plasticity 11 (8), 971 – 989.

Crépin, J., Bretheau, T., Caldemaison, D., 1996. Cavity growth and rupture of β–treated zirconium: A crystallographic model. Acta Mat. 44, 4927–4935.

Danas, K., Ponte Castañeda, P., 2009. A finite-strain model for anisotropic viscoplastic porous media: I-Theory. Eur. J. Mechanics A/Solids 28, 387–401.

DeBotton, G., Ponte Castañeda, P., 1995. Variational estimates for the creep behaviour of polycrystals. Proc. R. Soc. London Ser. A-Math. Phys. Sci. 448, 121–142.

Dubuisson, P., 2011. Le gonflement des aciers austénitiques. Revue de Métallurgie 108, 33–37.

Fabrègue, D., Pardoen, T., 2008. A constitutive model for elastoplastic solids containing primary and secondary voids. J. Mech. Phys. Solids 56, 719–741.

Faleskog, J., Gao, X., Shih, C., 1998. Cell model for nonlinear fracture analysis — I. Micromechanics calibration. Int. J. Frac. 89, 355–373.

Faleskog, J., Shih, C., 1997. Micromechanics of coalescence — I. Synergistic effects of elasticity, plastic yielding and multi–size–scale voids. J. Mech. Phys. Solids 45 (1), 21–50.

Foerch, R., Besson, J., Cailletaud, G., Pilvin, P., 1997. Polymorphic constitutive equations in finite element codes. Computer Methods in Applied Mechanics and Engineering 141, 355–372.

Foster, J. P., Strain, R. V., 1974. Empirical swelling equations for solution-annealed type 304 stainless steel. Nuclear Technology, 93–98.

Fritzen, F., Forest, S., Boehlke, T., Kondo, D., Kanit, T., 2012. Computational homogenization of elasto-plastic porous metals. Int. J. Plasticity 29, 102–119.

Gan, Y., Kysar, J., 2007. Cylindrical void in a rigid-ideally plastic single crystal III: Hexagonal close-packed crystal. Int. J. Plasticity 23 (4), 592–619.

Gan, Y., Kysar, J., Morse, T., 2006. Cylindrical void in a rigid-ideally plastic single crystal II: Experiments and simulations. Int. J. Plasticity 22, 39–72.

Gao, X., Faleskog, J., Shih, C., 1998. Cell model for nonlinear fracture analysis — ii. fracture–process calibration and verification. Int. J. Frac. 89, 375–398.

Goldstein, H., Poole, C., Safko, J., 2002. Classical mechanics. Third Edition. Addison Wesley.

Gologanu, M., Leblond, J.-B., 1993. Approximate models for ductile metals containing non-spherical voids - Case of axisymmetric prolate ellipsoidal cavities. J. Mech. Phys. Solids 41, 1723–1754.

Gurson, A., 1977. Continuum theory of ductile rupture by void nucleation and growth: Part I—Yield criteria and flow rules for porous ductile media. J. Engng Mater. Technol. 99, 2–15.

Ha, S., Kim, K., 2010. Void growth and coalescence in F.C.C. single crystals. Int. J. Solids Structures 52 (7), 863 – 873.

Huang, M., Li, Z., Wang, C., 2007. Discrete dislocation dynamics modelling of microvoid growth and its intrinsic mechanism in single crystals. Acta Mat. 55, 1387–1396.

Huang, M., Zhao, L., Tong, J., 2012. Discrete dislocation dynamics modelling of mechanical deformation of nickel-based single crystal superalloys. Int. J. Plasticity 28, 141–158.

Hussein, M., Borg, U., Niordson, C., Deshpande, V., 2008. Plasticity size effects in voided crystals. J. Mech. Phys. Solids 56, 114–131.

Koplik, J., Needleman, A., 1988. Void growth and coalescence in porous plastic solids. Int. J. Solids Structures 24 (8), 835 – 853.

Kuna, M., Sun, D. Z., 1996. Three-dimensional cell model analyses of void growth in ductile materials. Int. J. Frac. 81 (3), 235 – 258.

Kysar, J., Gan, Y., Mendez-Arzuza, G., 2005. Cylindrical void in a rigid-ideally plastic single crystal. Part I: Anisotropic slip line theory solution for face-centered cubic crystals. Int. J. Plasticity 21 (8), 1481–1520.

Lebensohn, R., Idiart, M., Ponte Castañeda, P., Vincent, P.-G., 2011. Dilatational viscoplasticity of polycrystalline solids with intergranular cavities. Phil. Mag. 91 (22), 3038 – 3067.

Leblond, J., Perrin, G., Suquet, P., 1994. Exact results and approximate models for porous viscoplastic solids. Int. J. Plasticity 10 (3), 213 – 235.

Lecarme, L., Tekoğlu, C., Pardoen, T., 2011. Void growth and coalescence in ductile solids with stage III and stage IV strain hardening. Int. J. Plasticity 27 (8), 1203–1223.

Liu, W., He, Z., Tang, J., Hu, Z., Cui, D., 2012. The effects of load condition on void coalescence in FCC single crystals. Comput. Mat. Sci. 60, 66–74.

Liu, W., Huang, H., Tang, J., 2010. FEM simulation of void coalescence in FCC crystals. Comput. Mat. Sci. 50, 411–418.

Liu, W. H., Zhang, X. M., Tang, J. G., Du, Y. X., 2007. Simulation of void growth and coalescence behavior with 3d crystal plasticity theory. Comput. Mat. Sci. 40 (1), 130 – 139.

Liu, Y., Gilormini, P., Ponte Castañeda, P., 2005. Homogenization estimates for texture evolution in halite. Tectonophys 406, 179–195.

Mc Clintock, F., 1968. A criterion for ductile fracture by the growth of holes. J. App. Mech. 35, 363–371.

Monchiet, V., Cazacu, O., Charkaluk, E., Kondo, D., 2008. Macroscopic yield criteria for plastic anisotropic materials containing spheroidal voids. Int. J. Plasticity 24, 1158 – 1189.

Monchiet, V., Charkaluk, E., Kondo, D., 2007. An improvement of gurson-type models of porous materials by using eshelby-like trial velocity fields. C. R. Acad. Sci. Paris 335 (1), 32 – 41.

Needleman, A., 1972. Void growth in an elastic-plastic medium. J. Applied Mech. 39 (4), 964 – 970.

Pardoen, T., Hutchinson, J. W., 2000. An extended model for void growth and coalescence. J. Mech. Phys. Solids 48 (12), 2467 – 2512.

Pineau, A., Pardoen, T., 2007. Failure mechanisms of metals. Chapter 6. Elsevier.

Ponte Castañeda, P., 1991. The effective mechanical properties of nonlinear isotropic composites. J. Mech. Phys. Solids 39 (1), 45 – 71.

Ponte Castañeda, P., 1992a. New variational principles in plasticity and their application to composite materials. J. Mech. Phys. Solids 40 (8), 1757 – 1788.

Ponte Castañeda, P., 1992b. A new variational principle and its application to nonlinear heterogeneous systems. SIAM J. Appl. Math. 52 (5), 1321 – 1341.

Ponte Castañeda, P., Suquet, P., 1998. Nonlinear composites. Advances in applied mechanics 34, 171–302.

Ponte Castañeda, P., Zaidman, M., 1996. The finite deformation of nonlinear composite materials -I. Instantaneous constitutive relations. Int. J. Solids Structures 33 (9), 1271 – 1286.

Potirniche, G., Horstemeyer, M., Wagner, G., Gullett, P., 2006. A molecular dynamics study of void growth and coalescence in single crystal nickel. Int. J. Plasticity 22, 257–278.

Quinn, D. F., Connolly, P. J., Howe, M. A., McHugh, P. E., 1997. Simulation of void growth in wc-co hardmetals using crystal plasticity theory. Int. J. Mech. Sci. 39 (2), 173 – 183.

Renault, A., Malaplate, J., Pokor, C., Gavoille, P., 2011. TEM and EFTEM characterization of solution annealed 304l stainless steel irradiated in PHENIX, up to 36 dpa and at 390°C. J. Nucl. Mat. 421, 124–131.

Rice, J., Tracey, D., 1969. On the ductile enlargement of voids in triaxial stress fields. J. Mech. Phys. Solids 17, 201–217.

Schacht, T., Untermann, N., Steck, E., 2003. The influence of crystallographic orientation on the deformation behaviour of single crystals containing microvoids. Int. J. Plasticity 19, 1605–1626.

Segurado, J., Llorca, J., 2009. An analysis of the size effect on void growth in single crystals using discrete dislocation dynamics. Acta Mat. 57, 1427–1436.

Segurado, J., Llorca, J., 2010. Discrete dislocation dynamics analysis of the effect of lattice orientation on void growth in single crystals. Int. J. Plasticity 26, 806–819.

Seran, J., Le Naour, L., Grosjean, P., Hugon, M., Carteret, Y., Maillard, A., 1984. Swelling and microstructure of neutron-irradiated Ti-modified type 316 stainless steel. Proc. of the 12th Int. Conf. on Effects of Radiation on Materials (Williamsburg 1984), ASTM STP 870, 233–247.

Steglich, D., Brocks, W., 1997. Micromechanical modelling of the behaviour of ductile materials including particles. Comput. Mat. Sci. 9, 7–17.

Steglich, D., Siegmund, T., Brocks, W., 1999. Micromechanical modeling of damage due to particle cracking in reinforced metals. Comput. Mat. Sci. 16, 404–413.

Tang, T., Kim, S., Horstemeyer, M., 2010a. Fatigue crack growth in magnesium single crystals under cyclic loading: Molecular dynamics simulation. Comput. Mat. Sci. 48, 426–439.

Tang, T., Kim, S., Horstemeyer, M., 2010b. Molecular dynamics simulations of void growth and coalescence in single crystal magnesium. Acta Mat. 58, 4742–4759.

Traiviratana, S., Bringa, E., Benson, D., Meyers, M., 2008. Void growth in metals: Atomistic calculations. Acta Mat. 56, 3874–3886.

Tvergaard, V., 1981. Influence of voids on shear band instabilities under plane strain conditions. Int. J. Frac. 17 (4), 389 – 407.

Tvergaard, V., 1982. On localization in ductile materials containing spherical voids. Int. J. Frac. 18 (4), 237 – 252.

Tvergaard, V., Needleman, A., 1984. Analysis of the cup–cone fracture in a round tensile bar. Acta Metall. 32, 157–169.

Wang, Y., Yue, Z., Stein, M., 2006. Experimental and finite element study of void growth in nickel-base single crystal superalloys. Rare Metal Mat. Eng. 35 (1), 39–42.

Worswick, M. J., Pick, R. J., 1990. Void growth and constitutive softening in a periodically voided solid. J. Mech. Phys. Solids 38 (5), 601 – 625.

Yerra, S. K., Tekoglu, C., Scheyvaerts, F., Delannay, L., van Houtte, P., Pardoen, T., 2010. Void growth and coalescence in single crystals. Int. J. Solids Structures 47 (7-8), 1016 – 1029.

Yu, Q. M., Hou, N. X., Yue, Z. F., 2010. Finite element analysis of void growth behavior in nickel-based single crystal superalloys. Comput. Mat. Sci. 48 (3), 597 – 608.

Zhang, K. S., Bai, J. B., François, D., 1999. Ductile fracture of materials with high void volume fraction. Int. J. Solids Structures 36 (23), 3407 – 3425.

Zhao, K., Chen, C., Shen, Y., Lu, T., 2009. Molecular dynamics study on the nano-void growth in face-centered cubic single crystal copper. Comput. Mat. Sci. 46, 749–754.

List of Tables

List of Figures

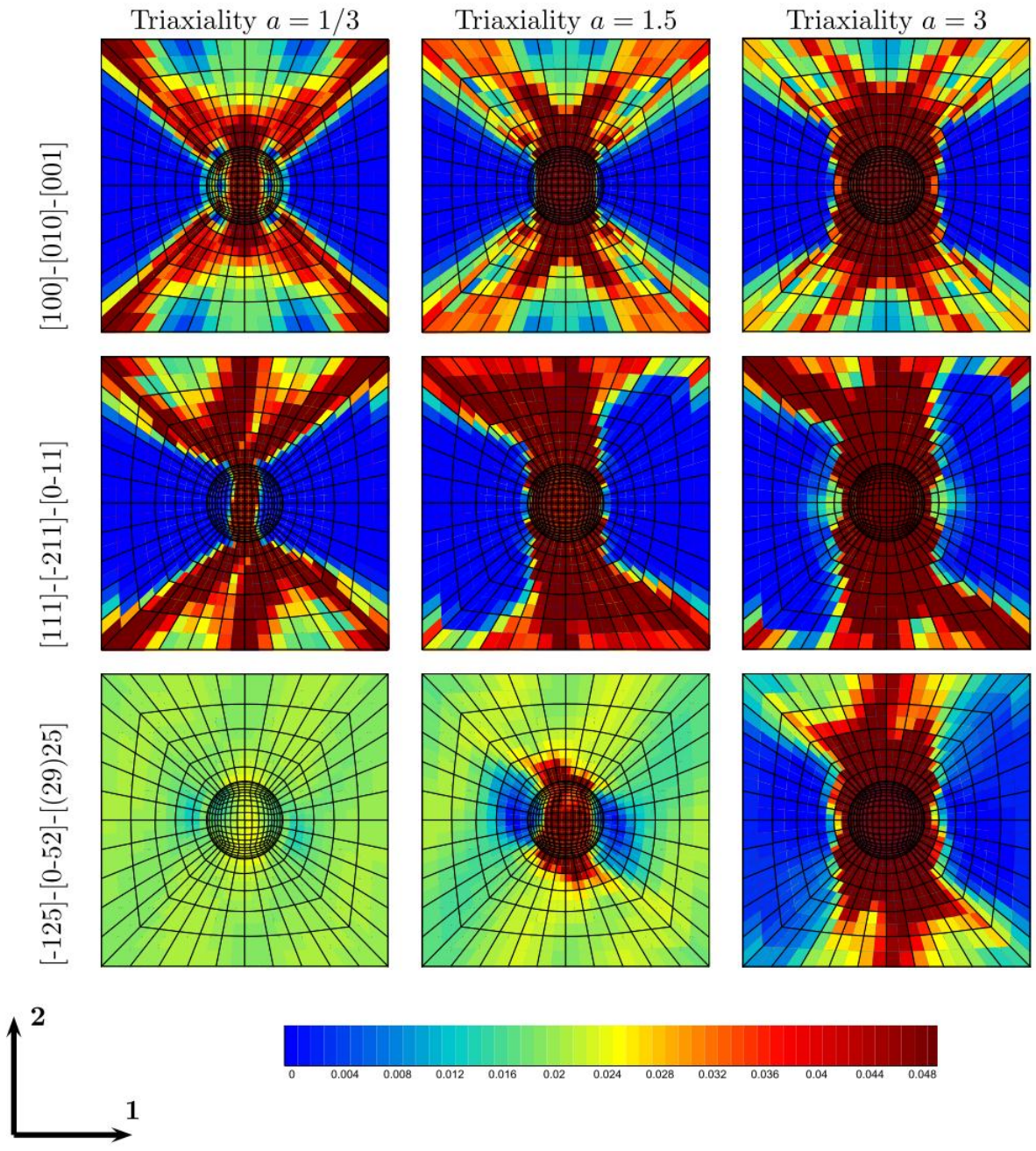

Figure 17: Fields of cumulative plastic slip γ_{cum} on all slip systems in the **1–2** plane cross-section of the unit cell, shown on non-deformed meshes, for three different orientations and three different triaxialities for an overall plastic deformation $E^p_{11} = 0.01$. The porosity is $f = 0.01$.

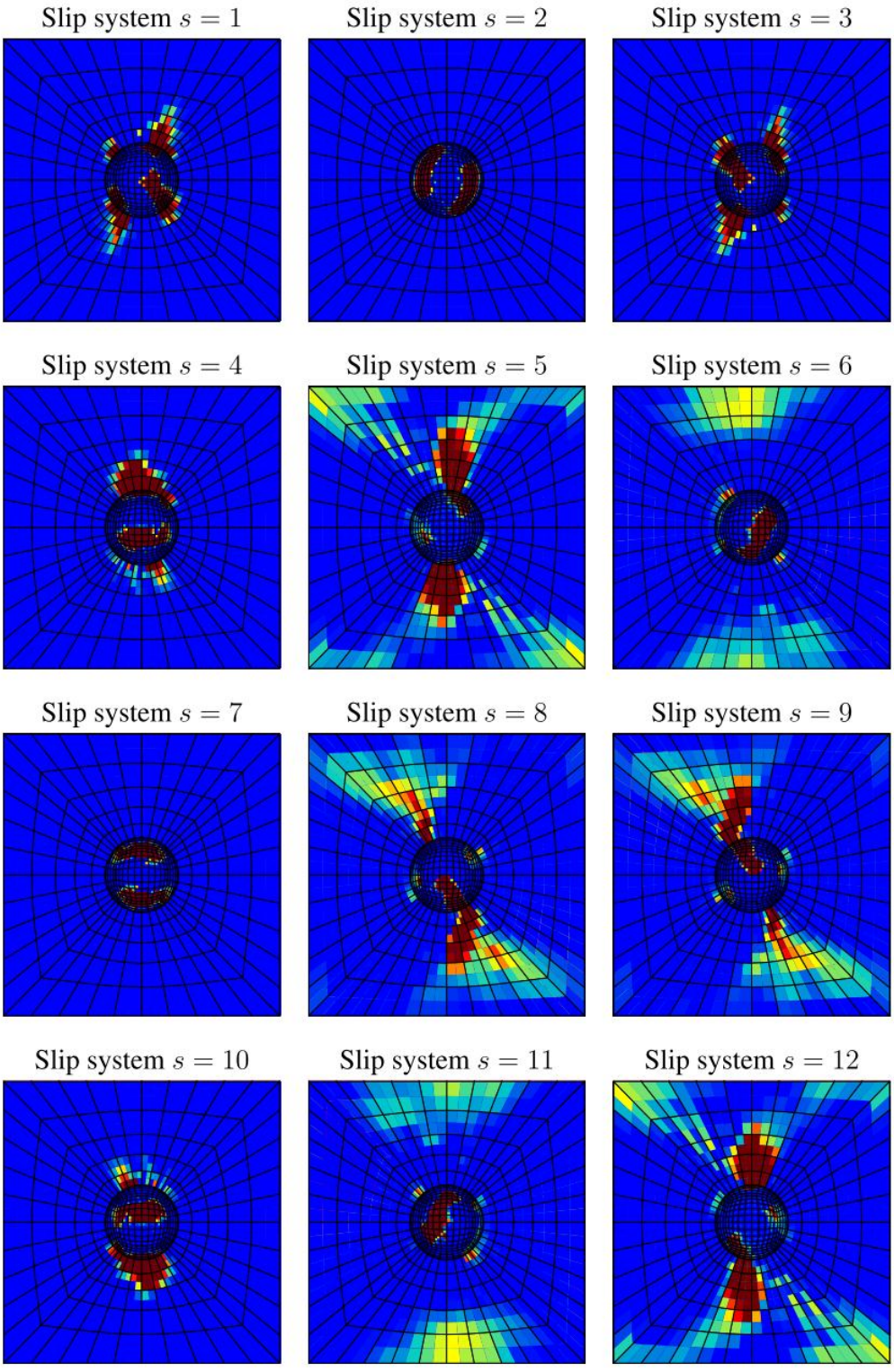

Figure 18: Fields of the amount of slip γ^s on all slip systems in the **1–2** plane cross-section of the unit cell, for the orientation $[111] - [\bar{2}11] - [0\bar{1}1]$ with an imposed triaxiality level of 1.5, shown on non-deformed meshes, for an overall plastic deformation $E^p_{11} = 0.01$. The porosity is $f = 0.01$. The color scale is the same as in Fig. 17.

4.3 Implémentation numérique du modèle monocristallin poreux dans le code ZéBuLoN

Après avoir développé le critère de plasticité pour un monocristal poreux, le modèle monocristallin poreux couplé doit être implémenté dans le code ZéBuLoN en l'adaptant au modèle cristallin déjà implémenté en grandes transformations présenté dans le **Chapitre 2**. On garde toujours la décomposition multiplicative du tenseur gradient de la transformation $\underline{\underline{F}} = \underline{\underline{E}} \cdot \underline{\underline{P}}$. L'objectif final est d'évaluer l'effet de la présence des cavités sur le comportement mécanique des matériaux irradiés. On rappelle ici le critère de plasticité pour un monocristal poreux proposé dans la **Section 4.2**, en utilisant les notations correspondantes au formalisme en grandes transformations :

$$\Phi = \left(\frac{\tau^{s2}}{\tau_s^{*2}} + \alpha \frac{2}{45} f \frac{\sigma_{eq}^2}{\tau_s^{*2}} \right) + 2q_1 f \cosh\left\{ q_2 \sqrt{\frac{3}{20}} \frac{\sigma_m}{\tau_s^*} \right\} - 1 - q_1^2 f^{2} \overset{\text{def. } \tau_s^*}{=} 0 \qquad \text{Équation 4.8}$$

avec τ^s la cission résolue de la matrice, τ_s^* la cission résolue équivalente du matériau poreux, σ_{eq} la contrainte équivalente de von Mises, σ_m la contrainte hydrostatique, f la porosité et α, q_1 et q_2 les coefficients du modèle.

Notons que τ^s, σ_{eq} et σ_m utilisés dans le critère de plasticité sont obtenus à partir du tenseur de contrainte décrit par le tenseur de Mandel $\underline{\underline{M}}$ dans la configuration isocline relâchée, ce qui nous permet d'appliquer la loi de Schmid, ainsi que la loi cristalline présentée ci-après.

En calculant le développement limité d'ordre 1 de l'**Équation 4.8**, on peut obtenir l'expression approximative de τ_s^* :

$$\tau_s^* = \frac{\sqrt{900\tau^{s2} + 40\alpha f \sigma_{eq}^2 + 135 q_1 f q_2^2 \sigma_m^2}}{30(1 - q_1 f)} \qquad \text{Équation 4.9}$$

La valeur de τ_s^* obtenue dans l'**Équation 4.9** permet de fournir un point de départ pour calculer la valeur exacte de τ_s^* (avec $\tau_s^*>0$) soit par la méthode de Newton-Raphson, soit par la méthode de dichotomie, via les deux routines existantes dans le code ZéBuLoN.

Dans un premier temps, l'évolution de la forme des cavités n'est pas prise en compte dans notre modèle. Du fait que le critère développé ci-dessus est implémenté en grandes transformations, en supposant que le matériau dense n'est pas compressible et que le changement de volume est seulement dû à la déformation plastique (celui dû à la déformation élastique n'est pas un facteur d'endommagement), on obtient explicitement l'expression de la porosité :

$$\det P = \frac{V_p}{V_0} = \frac{V_m/(1-f)}{V_0} = \frac{1-f_0}{1-f} \Rightarrow f = 1 - \frac{1-f_0}{\det P}, 0 \le f \le 1 \qquad \text{Équation 4.10}$$

avec f_0 la fraction volumique initiale de cavité.

La loi d'écoulement adaptée aux matériaux poreux s'écrit alors :

$$\dot{\gamma}^s = \left\langle \frac{\tau_s^* - \tau_c^s}{K_0} \right\rangle^n \qquad \text{Équation 4.11}$$

Il est à noter que la cission résolue effective τ_s^* n'est pas signée, ce qui implique une loi d'écoulement non-signée (**Équation 4.11**). Par conséquent, les équations décrivant les évolutions des densités de dislocations et de boucles de Frank n'ont pas besoin de prendre en compte le signe de $\dot{\gamma}^s$. On obtient donc pour les matériaux poreux à l'état irradié :

- Modèle de **« la racine de la somme »** poreux : à partir de l'**Équation 2.20**

$$\dot{r}_D^s = \dot{\gamma}^s \left(\frac{\sqrt{\sum_u b^{su} r_D^u + K_{dl} \sum_p r_L^p}}{\kappa} - G_c r_D^s \right) \qquad \text{Équation 4.12}$$

- Modèle de **« la somme des racines »** poreux : à partir de l'**Équation 2.23**

$$\dot{r}_D^s = \dot{\gamma}^s \left(\frac{\sqrt{\sum_u b^{su} r_D^u} + \sqrt{K_{dl} \sum_p r_L^p}}{\kappa} - G_c r_D^s \right) \qquad \text{Équation 4.13}$$

- Evolution de $\dot{r}_L^p$ identique pour les deux modèles présentés ci-dessus : à partir de l'**Équation 2.21**

$$\dot{r}_L^p = -A_L \left(\sum_{s \in plan(p)}^{3} r_D^s \right) \left(r_L^p - r_L^{sat} \right) \left(\sum_{s \in plan(p)}^{3} \dot{\gamma}^s \right) \qquad \text{Équation 4.14}$$

Le tenseur gradient du vecteur vitesse associé au glissement plastique en grandes déformations $\underline{\underline{L}}^p$ en prenant en compte la porosité s'exprime par :

$$\underline{\underline{L}}^p = (1-f) \sum_{s=1}^{12} \dot{\gamma}^s \underline{\underline{n}}^s, \text{ avec } \underline{\underline{n}}^s = \frac{\partial \tau_s^*}{\partial \underline{\underline{\sigma}}} \qquad \text{Équation 4.15}$$

Notons que $\underline{\underline{n}}^s$ représente la direction de l'écoulement pour un matériau poreux, différente de celle pour un matériau sain $\underline{\underline{N}}^s$ qui est fixée par la loi de Schmid.

En imposant que la variation de la surface de charge reste nulle $\delta\Phi = 0$ pour une variation de $\underline{\underline{\sigma}}$, la variation de τ_s^* est donnée par :

$$\delta\Phi = \frac{\partial \Phi}{\partial \underline{\underline{\sigma}}} \cdot \delta \underline{\underline{\sigma}} + \frac{\partial \Phi}{\partial \tau_s^*} \cdot \delta \tau_s^* = 0 \qquad \text{Équation 4.16}$$

A l'aide de l'**Équation 4.13**, la direction de l'écoulement peut être donnée par :

$$\underline{\underline{n}}^s = \frac{\partial \tau_s^*}{\partial \underline{\underline{\sigma}}} = -\frac{1}{H} \cdot \underline{\underline{Q}}, \text{ avec } \underline{\underline{Q}} = \frac{\partial \Phi}{\partial \underline{\underline{\sigma}}} \text{ et } H = \frac{\partial \Phi}{\partial \tau_s^*} \qquad \text{Équation 4.17}$$

Les expressions de $\underline{\underline{M}}$ et H peuvent être calculées et présentées respectivement comme suit :

$$\underline{\underline{Q}} = \frac{\partial \Phi}{\partial \underline{\underline{\sigma}}} = \frac{2\tau^s}{\tau_s^{*2}} \underline{\underline{N}}^s + \frac{2}{15} \frac{\alpha f}{\tau_s^{*2}} \underline{\underline{s}} + \frac{2}{3} \sqrt{\frac{3}{20}} q_1 q_2 f \frac{\sinh\left(q_2 \sqrt{3/20}\, \sigma_m / \tau_s^*\right)}{\tau_s^*} \underline{\underline{1}}$$

$$H = \frac{\partial \Phi}{\partial \tau_s^*} = -2\frac{\tau^{s2}}{\tau_s^{*3}} - \frac{4}{45} \alpha f \frac{\sigma_{eq}^2}{\tau_s^{*3}} - 2\sqrt{\frac{3}{20}} q_1 q_2 f \frac{\sigma_m}{\tau_s^{*2}} \sinh\left(q_2 \sqrt{\frac{3}{20}} \frac{\sigma_m}{\tau_s^*}\right) \qquad \text{Équation 4.18}$$

avec $\underline{\underline{s}}$ le déviateur du tenseur des contraintes et $\underline{\underline{1}}$ le tenseur d'identité d'ordre 2.

Les composantes dans la matrice jacobienne adaptées aux matériaux poreux sont mises à jour dans l'**Annexe II. 1**. Par contre, le calcul de la matrice tangente cohérente reste inchangé.

4.4 Tests simples sur des monocristaux non-irradié et irradié

Suite à l'implémentation du modèle monocristallin poreux dans le code ZéBuLoN, des tests simples sont réalisés afin de vérifier l'implémentation et de réaliser une étude préliminaire des influences de l'orientation cristallographique et de la porosité sur le comportement mécanique des matériaux non-irradié et irradié.

Les calculs numériques en traction simple sont réalisés sur un seul élément fini suivant 5 orientations cristallographiques représentatives pour les matériaux non-irradié et irradié avec les mêmes conditions de tests que celles utilisées dans la **Section 2.5.2**. Les paramètres de la loi cristalline sont pris dans le **Tableau 2.5** sauf que les coefficients de la matrice d'interaction a^{su} sont choisis identiques a_i = 0.124 (i = 1…6) afin d'éviter l'apparition de l'instabilité numérique. De plus, pour le matériau irradié, l'effet d'avalanche est également introduit dans les tests avec les paramètres τ_a = 20MPa et γ_a=0.005. Les résultats obtenus pour une direction de traction suivant [001] sont présentés sur la **Figure 4.1**. Les résultats des calculs numériques suivant les autres directions de traction sont présentés dans l'**Annexe II. 2**.

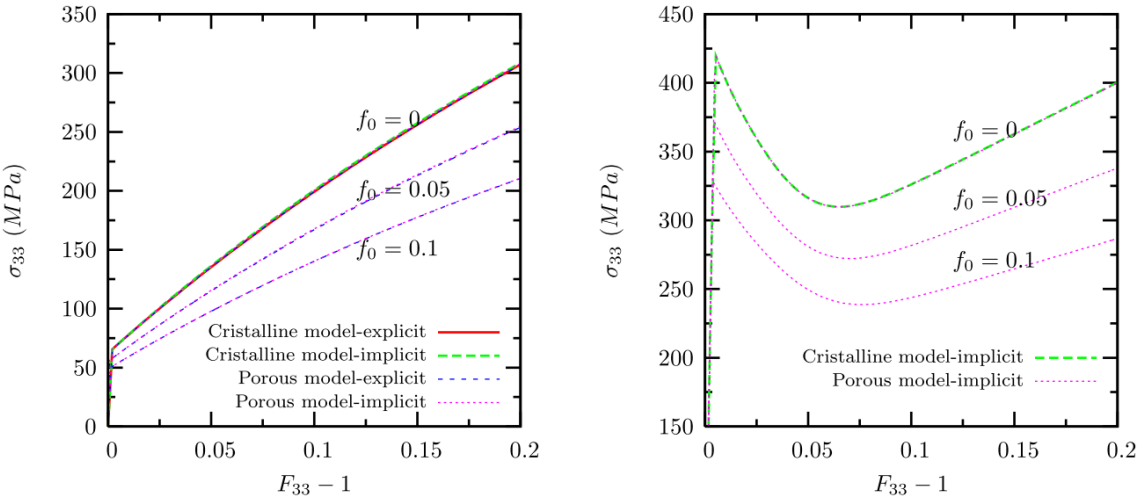

Figure 4.1 : Courbes de traction obtenues pour les matériaux (a) non-irradié et (b) irradié, sans et avec le modèle monocristallin poreux, pour différents niveaux de porosité.

D'après tous les résultats présentés ci-dessus, on peut constater que le modèle monocristallin poreux permet de décrire l'effet de porosité sur un monocristal en présence de cavités, en prenant en compte la cristallographie du monocristal. L'utilisation de ce modèle poreux ne pose pas de problème d'instabilité numérique par rapport au modèle cristallin dense. Les évolutions de porosité suivant différentes directions de traction sont tracées sur la **Figure 4.2**. Du fait que ces résultats sont obtenus à partir des calculs de traction uniaxiale, la croissance des cavités n'est pas très importante. Cependant, une influence de l'anisotropie due à la cristallographie du monocristal sur la croissance des cavités peut être observée. Celle-ci reste à vérifier à partir des calculs de cellules élémentaires.

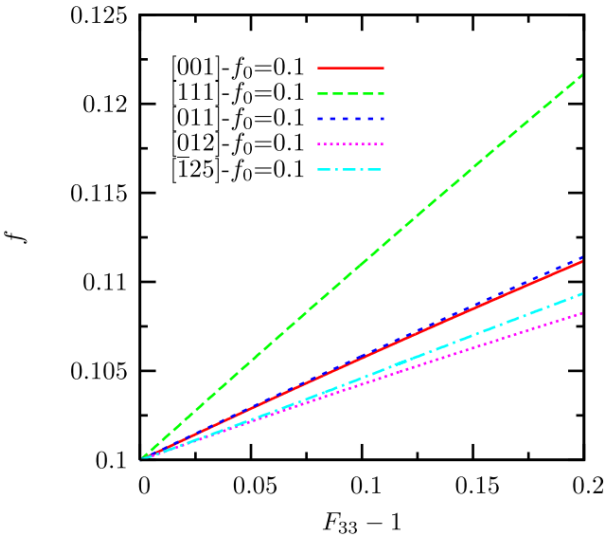

Figure 4.2 : Evolutions de porosité pour différentes orientations cristallographiques. Les résultats sont obtenus à partir des calculs de traction uniaxiale.

4.5 Bilan et conclusions partielles

Basé sur l'approche variationnelle de type Hashin-Shtrikman d'un monocristal linéaire de comparaison [Debotton (1995) et Bugat (2000)], un modèle de type Gurson pour les monocristaux poreux a été développé. Un terme quadratique de la cission résolue τ^s permettant de décrire l'anisotropie liée à la cristallographie intervient dans le critère de plasticité proposé. 3 coefficients α, q_1 et q_2 sont introduits dans le critère et ajustés sur un grand nombre des calculs numériques réalisés sur une cellule monocristalline tri-dimensionnelle parfaitement plastique contenant une cavité sphérique au milieu de la cellule. Les effets de l'orientation cristallographique, de la triaxialité et de la porosité sont étudiés. D'après les résultats obtenus, on peut conclure que le critère de plasticité développé est capable de prédire la surface de charge d'un monocristal poreux pour tous les niveaux de triaxialité, en tenant compte des directions du chargement principale et secondaire, ainsi que l'effet de la porosité. Ce travail a fait l'objet d'un article qui a été soumis à « International Journal of Solids and Structures » en 2012.

D'après les résultats préliminaires obtenus, dans un premier temps, on peut conclure que le modèle monocristallin poreux a été bien implémenté avec les méthodes d'intégration explicite et implicite dans le code de calcul ZéBuLoN. Ce modèle poreux prend en compte les effets de l'orientation cristallographique et de la porosité. L'expression de l'évolution de la porosité est donnée explicitement à l'aide du formalisme en grandes transformations. Afin d'étudier précisément l'effet de la porosité sur l'écrouissage du matériau, ainsi que la croissance et la coalescence des cavités au sein d'un monocristal, une loi d'évolution de la forme des cavités pour les monocristaux poreux doit être proposée, en comparant les résultats obtenus à partir de la cellule monocristalline poreuse.